iScience

CellPress
OPEN ACCESS

Article

Chemically Programmed Vaccines: Iron Catalysis in Nanoparticles Enhances Combination Immunotherapy and Immunotherapy-Promoted Tumor Ferroptosis

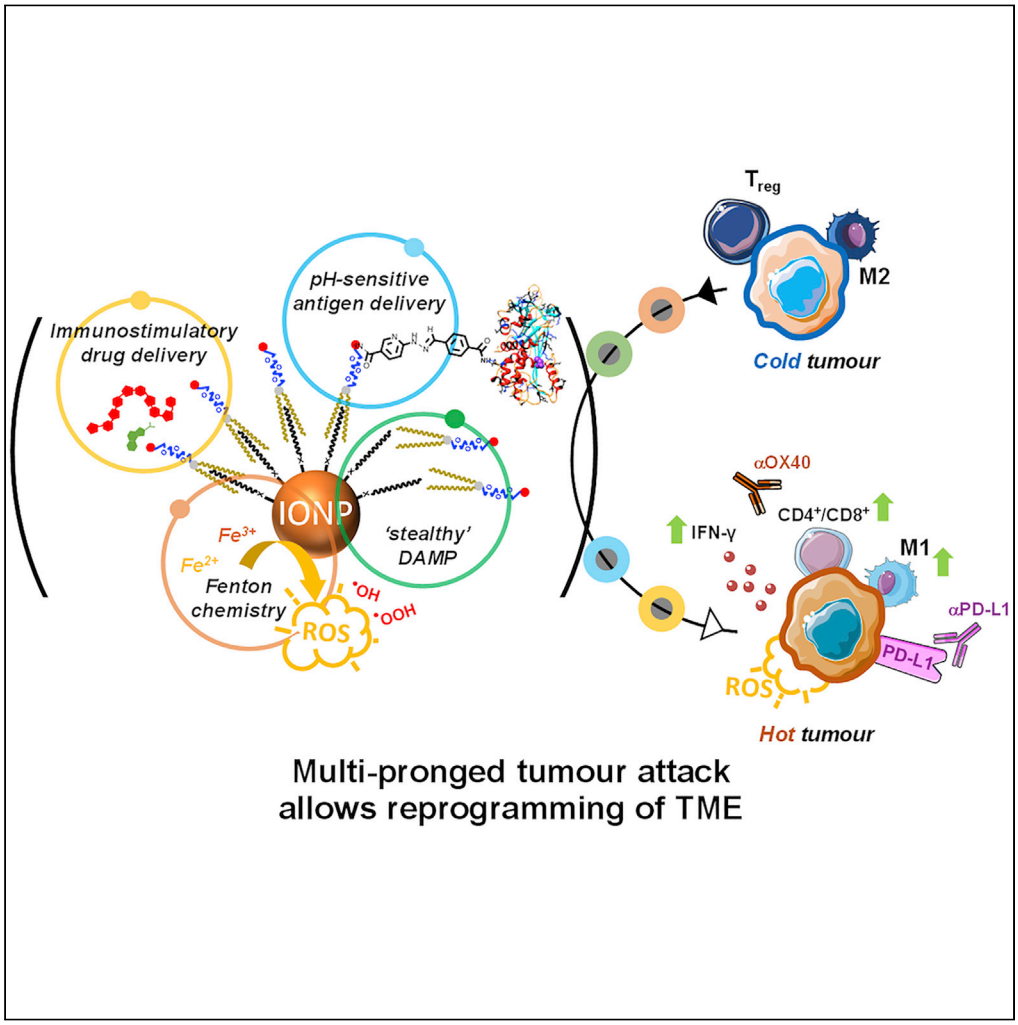

Ane Ruiz-de-Angulo, Marc Bilbao-Asensio, James Cronin, ..., Rhiannon Beadman, Kepa Zamacola Bascarán, Juan C. Mareque-Rivas

aruizdeangulo@cicbiogune.es (A.R.-d.-A.)
juan.mareque-rivas@swansea.ac.uk (J.C.M.-R.)

HIGHLIGHTS

Chemistry-enabled IONVs offer a generalizable approach for enhanced therapeutic effects

The IONVs are chemically programmed with catalytic iron and reversible bonds

IONVs take advantage of TME metabolism to increase ferroptosis in tumor cells

Immune checkpoint antibodies improve IONVs and vice versa

Ruiz-de-Angulo et al., iScience *23*, 101499
September 25, 2020 © 2020 The Authors.
https://doi.org/10.1016/j.isci.2020.101499

iScience

CellPress
OPEN ACCESS

Article

Chemically Programmed Vaccines: Iron Catalysis in Nanoparticles Enhances Combination Immunotherapy and Immunotherapy-Promoted Tumor Ferroptosis

Ane Ruiz-de-Angulo,[3,*] Marc Bilbao-Asensio,[1] James Cronin,[4] Stephen J. Evans,[4] Martin J.D. Clift,[4] Jordi Llop,[2] Irene V.J. Feiner,[2] Rhiannon Beadman,[4] Kepa Zamacola Bascarán,[2] and Juan C. Mareque-Rivas[1,5,*]

SUMMARY

Immunotherapy has yielded impressive results, but only for a minority of patients with cancer. Therefore, new approaches that potentiate immunotherapy are a pressing medical need. Ferroptosis is a newly described type of programmed cell death driven by iron-dependent phospholipid peroxidation via Fenton chemistry. Here, we developed iron oxide-loaded nanovaccines (IONVs), which, chemically programmed to integrate iron catalysis, drug delivery, and tracking exploiting the characteristics of the tumor microenvironment (TME), improves immunotherapy and activation of ferroptosis. The IONVs trigger danger signals and use molecular disassembly and reversible covalent bonds for targeted antigen delivery and improved immunostimulatory capacity and catalytic iron for targeting tumor cell ferroptosis. IONV- and antibody-mediated TME modulation interfaced with imaging was important toward achieving complete eradication of aggressive and established tumors, eliciting long-lived protective antitumor immunity with no toxicities. This work establishes the feasibility of using nanoparticle iron catalytic activity as a versatile and effective feature for enhancing immunotherapy.

INTRODUCTION

It is becoming apparent that the immune system can be harnessed to treat cancer. One of the most promising new approaches is based on immune checkpoint inhibitors (ICIs), which re-invigorate the capacity of tumor antigen-specific T cells to attack the cancer (Wei et al., 2018). This immunotherapy has enabled some patients to produce an effective and durable antitumor response. However, the proportion of patients responding to single ICIs remains low (<20%) (Shields et al., 2017; Chen and Han, 2015). Despite efforts to develop combinatorial approaches that increase response rates, studies show minimal improvements in patient survival and/or greater toxicity, usually as a result of targeting redundant immune pathways (Moslehi et al., 2018; Messenheimer et al., 2017). Targeting immune checkpoints harnesses a pre-existing (ineffective) immune response of so-called immune "hot" tumors (Galon and Bruni, 2019) and is hampered by immune-related adverse effects (Friedman et al., 2016) and acquired drug resistance (Jenkins et al., 2018). Therefore, attractive strategies to improve the therapeutic index of ICI are based on the development of immunotherapy drug delivery technologies, and targeting non-redundant additional pathways, such as metabolic features of cancer, through combinatorial approaches (Riley et al., 2019; Doll et al., 2019).

Advances made in the understanding of the biology of cancer, biomedical engineering, and nanochemistry have enabled innovative treatment strategies, which when investigated in combination with immunotherapy show synergistic therapeutic effects in mouse models of cancer, but obstacles to their clinical translation remain. Combination with nanoparticle-enabled photodynamic therapy (PDT) (Ni et al., 2018) is limited by the light penetration depth, oxygen reliance, and systemic toxicity due to off-site drug accumulation (Lucky et al., 2015), whereas use of high-intensity focused ultrasound (HIFU) (Eranki et al., 2019) is also unsuitable for deep-seated tumors owing to attenuation of the ultrasound waves in deep tissue. Immunotherapy enhancement by photothermal ablation (PTA) and by magnetic hyperthermia (MHT) (Chao et al., 2019) require high local nanoparticle concentrations, which can cause severe damages to normal tissue in

[1]Department of Chemistry and Centre for NanoHealth, Swansea University, Singleton Park, Swansea SA2 8PP, UK

[2]Radiochemistry and Nuclear Imaging Laboratory, CIC BiomaGUNE, Paseo Miramón 182, San Sebastián 20014, Spain

[3]Chemical Immunology Laboratory, CIC BioGUNE, Building 801A, Derio 48160, Spain

[4]Swansea University Medical School, Institute of Life Science, Singleton Park, Swansea SA2 8PP, UK

[5]Lead Contact

*Correspondence: aruizdeangulo@cicbiogune.es (A.R.-d.-A.), juan.mareque-rivas@swansea.ac.uk (J.C.M.-R.)

https://doi.org/10.1016/j.isci.2020.101499

This is an open access article under the CC BY-NC-ND license (http://creativecommons.org/licenses/by-nc-nd/4.0/).

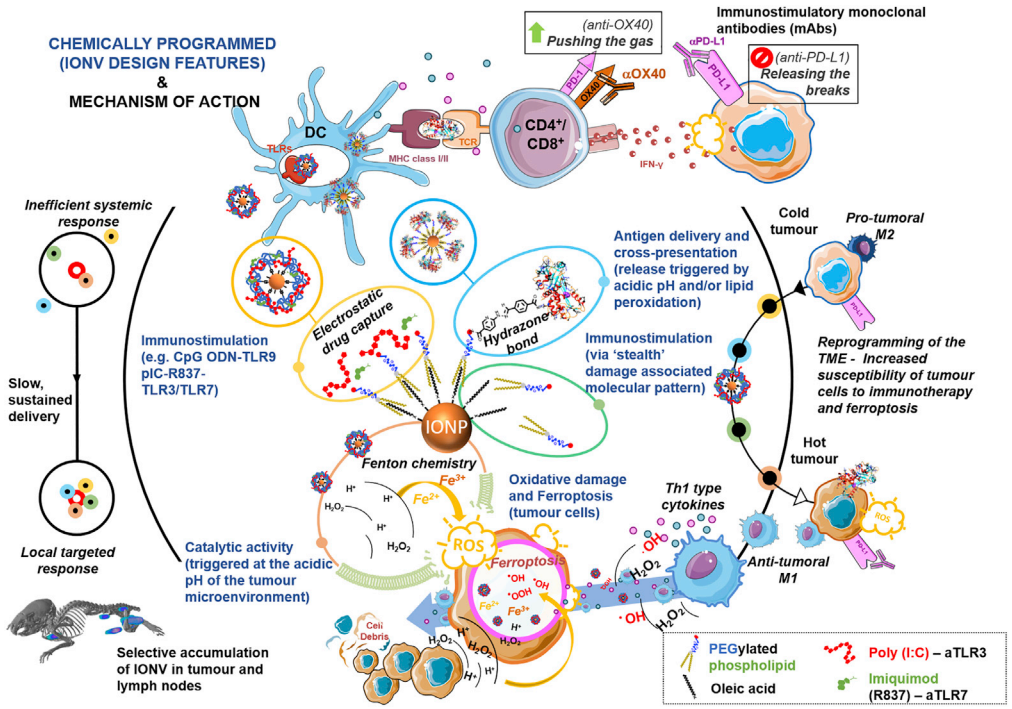

Scheme 1. Design, Mechanism and Features of IONVs

Design and mechanism of action of inherently therapeutic IONVs with chemically programmed multi-functional elements to activate and reprogram immune cells and cancer cells, harnessing the TME to sensitize tumors for immunotherapy and ferroptosis.

the tumor margins and induce tumor metastasis. Although iron oxide nanoparticle (IONP)-enabled ICI delivery applying external magnetic field has been reported in mice (Chiang et al., 2018), it is not currently feasible in targeting deep tumor tissue of human patients partly owing to lack of suitable magnetic systems (Shapiro et al., 2015). Consequently, there is an urgent need for developing approaches that address these challenges. Growing evidence implies that the tumor microenvironment (TME), which poses a significant obstacle to these approaches, may be targeted and harnessed to obtain substantial therapeutic benefits (Pitt et al., 2016; Anderson et al., 2017).

The immune component of the TME contains $CD4^+$ and $CD8^+$ T cells (regulatory T cells [T_{regs}] and exhausted effector T cells) and tolerogenic dendritic cells (DCs) and tumor-associated macrophages (Shiao et al., 2011; Gajewski et al., 2013). Intracellular communication in the TME is driven by a complex and dynamic network of signaling molecules such as cytokines and chemokines against a backdrop of specific metabolic alterations (hypoxia, low pH, nutrient deprivation, high content of H_2O_2, etc.). These features result in cancer cell metabolic reprogramming (Ward and Thompson, 2012) and an intrinsic vulnerability of cancer cells to a newly described form of regulated cell death termed ferroptosis (Yang and Stockwell, 2016). Ferroptosis, induced by oxidative stress and characterized by iron-dependent phospholipid peroxidation via chain reactions referred to as Fenton chemistry, offers a new way to target treatment-resistant cancers (Doll et al., 2019). We conceive here that iron oxide-filled nanovaccines (IONVs) can exploit the biochemical hallmarks of the TME for *in situ* "self-generation" of H_2O_2, which when converted by the IONV into highly toxic ROS, via Fenton chemistry and acting as peroxidase catalyst, drives and concentrates complementary or synergistic antitumor mechanisms in the TME. We chemically programmed the IONVs to provide (1) non-invasive imaging and effective delivery of combination therapy to the tumor and tumor draining lymph nodes (TDLNs), (2) nanoparticle-tuned disassembly to reveal "stealth" immunostimulatory features, (3) an iron oxide core that can artificially reprogram *in situ* pro-tumoral M2 macrophages into antitumor M1 macrophages (Li et al., 2019), and (4) improved tumor antigen cross-presentation by a pH-responsive hydrazone tumor antigen linkage strategy (Scheme 1). Importantly, since interferon gamma (IFN-γ) released from immunotherapy-activated $CD8^+$ T cells has recently been shown to trigger ferroptosis-specific lipid peroxidation in tumor cells (Wang et al., 2019), we utilize the IONV iron content

and peroxidase-like activity to sensitize tumor to ferroptosis, further stimulating the immunotherapy and overcoming immunotherapy resistance mechanisms.

In aggressive and established melanomas, we performed a screening of different immune adjuvants in nanoparticle-free vaccines and then sought to systematically assess and quantify how specific nanoparticle engineering design elements impact the responses to therapies. Finally, the combination of IONV- and antibody-mediated nuclear imaging and modulation of cell populations in the TME resulted in complete eradication of established tumors *in vivo*, eliciting long-lived protective antitumor immunity in treated mice with no observed toxicities. This work provides proof-of-concept demonstration of how iron and IONP-dependent catalytic activity can harness TME biochemical features to improve vaccination and immunotherapy activation of ferroptosis and potentially become one of the centerpieces for immunotherapy enhancement with nanomedicine.

RESULTS

Prophylactic and Therapeutic Implications of Different Toll-like Receptor Agonists

Toll-like receptor agonists (TLRa) have demonstrated potential for the treatment of cancer through direct and indirect activation of different leukocytes of the innate and adaptive immune systems (Schmidt, 2006). To use intrinsically therapeutic catalytic nanovaccines, we first performed a screening of different Tara's against highly aggressive melanoma tumors, which are characteristically difficult to treat or "cure" once large visible tumors have developed (B16-F10 cells expressing the xeno-antigen ovalbumin [OVA]). The prophylactic implications and efficacy of the TLRa as a vaccine adjuvant was studied by subcutaneously administering low doses (1–5 μg) with full-length OVA. The studies revealed the efficacy of targeting synergistic TLR signaling, achieved by combining imiquimod (R837, synthetic small molecule serving as TLR7-specific ligand) and polyIC (synthetic double-stranded RNA serving as a TLR3 agonist) (Figures 1A–1C), as well as the anti-melanoma protection achieved with unmethylated CG-enriched oligodeoxynucleotides (CpG ODNs), a TLR9 ligand. In comparison, the TLR4 agonists *Xcc*-LOS (*Xanthomonas campestris* lipooligosaccharides) (Traini et al., 2019) and LPS (lipopolysaccharide), and the detoxified ligand MPLA (monophosphoryl lipid A), successfully used as adjuvant in clinically approved vaccines and tested in several clinical trials for anti-cancer vaccines, were less effective at generating protective antitumor immunity (Cluff, 2009). In order to study the *in vivo* antitumor effects of these adjuvants, we subcutaneously implanted the melanoma tumor and after the tumor had become established (ca. 7 days), we administered the best-performing adjuvants (polyIC-R837 or CpG ODNs) and OVA. The potential of cisplatin chemotherapy to convert the tumor into a permissive site for the activation of an adaptive immune response within the tumor (Kang et al., 2013), even without administration of adjuvant, was also studied. Co-treatment with chemotherapy and tumor antigen administration led to slower tumor growth and longer survival compared with monotherapy (Figures 1D and 1E), indicating that priming of the tumor-specific immune response with chemotherapy is possible with OVA antigen delivery into the TME. However, although the generation of antitumor effects achieved by CpG ODNs and polyIC-R837 was with complete absence of systemic toxicity, the chemotherapy acting as vaccine adjuvant is accompanied by systemic toxicity and rapid weight loss initiated following the first injection, an effect that exacerbated with each dose (Figure 1F).

Improvement of Vaccination Efficacy Derived from Nanocarrier Design

Delivery of tumor antigens and vaccine adjuvants to the tumor and TDLNs is important to prime antitumor immunity and fight against tumor immune escape mechanisms. Hence, for safe and robust vaccination a strategy is to engineer nanocarriers that enable vaccine effective delivery to the lymph node microenvironment (Irvine et al., 2013; Storni et al., 2005). The adjuvant can help to convert the immunodormant ("cold") TME into an immunostimulatory ("hot") one while taking advantage of tumor-associated antigen drainage. Since various physicochemical properties can be tailored to enable effective drug delivery to lymph nodes, nanocarrier design is critical (Schudel et al., 2019).

We created PEG-phospholipid (PEG-PL)-stabilized IONP-bound oleates carrying adjuvant/antigen (IONVs), which led to micelles <100 nm with good stability for up to 2 weeks (Figures S2–S5).(Carion et al., 2007; Cobaleda-siles et al., 2014) We included the cationic lipid DOTAP to self-assemble polyIC and CpG upon mixing via electrostatic interactions between the positive charges of the lipid and the negative charges of the nucleic acid-based TLRas. The incorporation of R837 to IONVs was conducted by its intercalation into the polyIC dsRNA chain, forming polyIC-R837 complexes as shown in our previous work (Bocanegra Gondan et al., 2018). The model antigen OVA was successfully adsorbed by iron oxide

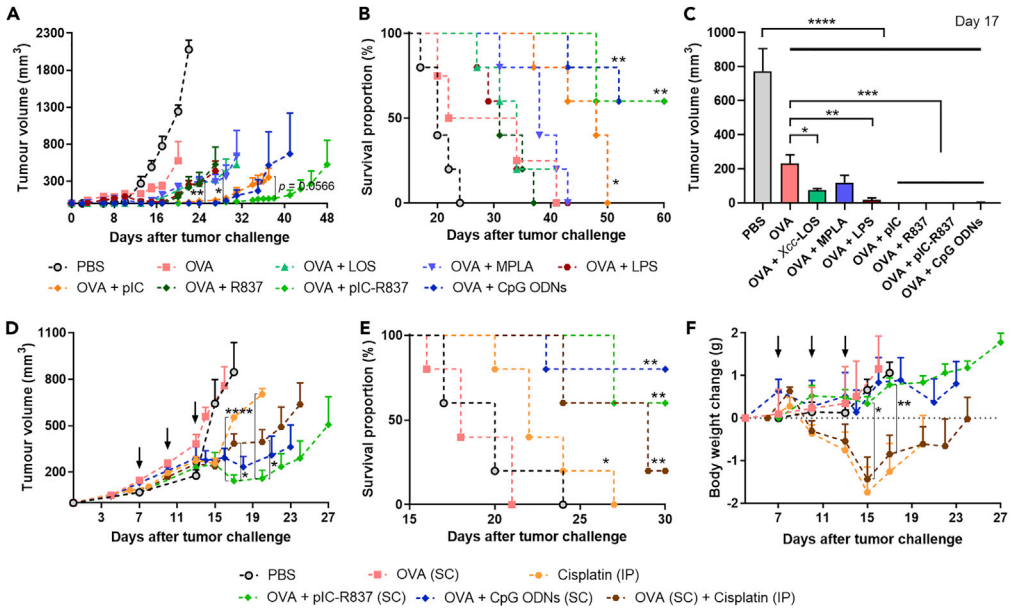

Figure 1. *In Vivo* Evaluation of the Effect of Vaccination with Different TLR Agonists and Cisplatin Chemotherapy as Adjuvants

(A–C) In the prophylactic approach, C57BL/6 mice (n = 5) were immunized subcutaneously on days 0 and 14 with 5 μg of OVA free or in combination with TLR4 agonists *Xcc*-LOS, MPLA, LPS (1 μg/mouse), TLR3 agonist pIC (4 μg/mouse), TLR7 agonist R837 (2 μg/mouse), pIC-R837 or TLR6 agonist CpG ODNs (5 μg/mouse). Mice were challenged with 3×10^5 B16-F10(OVA) cells in the right back on day 21 after first immunization. (A) Average tumor growth curves and (B) Kaplan-Meier survival curves. (C) Comparison of tumor volume of different experimental groups at day 17 after tumor challenge. The data show mean ± SEM from a representative experiment.

(D–F) To exploit for cancer therapy C57BL/6 mice (n = 5) were treated on days 7, 10, and 13 after B16-F10(OVA) cells injection in the right back. Animals were subcutaneously administered with 10 μg of OVA free or in combination with pIC-R837 (4 and 2 μg, respectively), CpG ODNs (10 μg), and cisplatin (intraperitoneal, 100 μg). In this last group, cisplatin was administered with 60 μg of OVA antigen subcutaneously, in order to mimic the literature. (D) Average tumor growth curves, (E) Kaplan-Meier survival curves, and (F) animal body weight change over the experiment. Arrows indicate the days of therapy administration. Data are shown as mean ± SEM. *$p < 0.05$, **$p < 0.01$, ***$p < 0.001$, ****$p < 0.0001$ by two-tailed unpaired Student's t test (A, D, and F), by log rank (Mantel-Cox) test against OVA (SC) group (B and E), and one-way ANOVA followed by Tukey's test (C). See also Figure S1.

nanoparticle-filled micelles (mIONPs) containing DSPE-cPEG(2000)-PL with COOH end groups exploiting the concept of "nanoparticle-protein corona"(Nguyen and Lee, 2017). To investigate the delivery of the IONVs to lymphatic tissues and tumor, we ^{67}Ga-radiolabeled the IONP surface exploiting the similarity between Ga(III) and Fe(III) as reported previously (Ruiz-De-Angulo et al., 2016). This smart organic synthesis-free process, which involves reaction of the readily obtained radiocation $[^{67}Ga][Ga(H_2O)_6]Cl_3$ (aq.) with the anionic IONVs at 70°C for 30 min followed by purification by ultracentrifugation, proceeded with very good yield (>80%; Figures 2A, 2B, and 2C). The ^{67}Ga-doped IONVs showed excellent stability, with less than 10% of the bound ^{67}Ga being released over 24 h even when challenged with 10^6-fold molar excess of DOTA chelator, and therefore suitability for *in vivo* tracking (Figure 2C).

SPECT/CT imaging results showed that these IONVs selectively accumulate in LNs and tumor up to 24 h (Figures 2D–2F and S6 and S7). Particles cleared from the injection site were excreted into the urine and accumulated at proximal and distal draining LNs within 3 h post injection (Figures 2D and S6), which is consistent with self-lymphatic delivery and confirms the lymphatic drainage from the tumor implantation site to tumor-draining lymph nodes (TDLNs). Therefore, the *in vivo* biodistribution experiments demonstrated IONVs are sufficiently small and stealthy to be rapidly taken up into lymphatic vessels and transit to the draining LN after subcutaneous (SC) injection.

To investigate the therapeutic efficacy of nanoparticle vaccination, mice were treated with non-covalently formed IONVs with the polyIC-R837 or CpG ODNs (Figure S8) adjuvant and OVA. The IONVs achieved

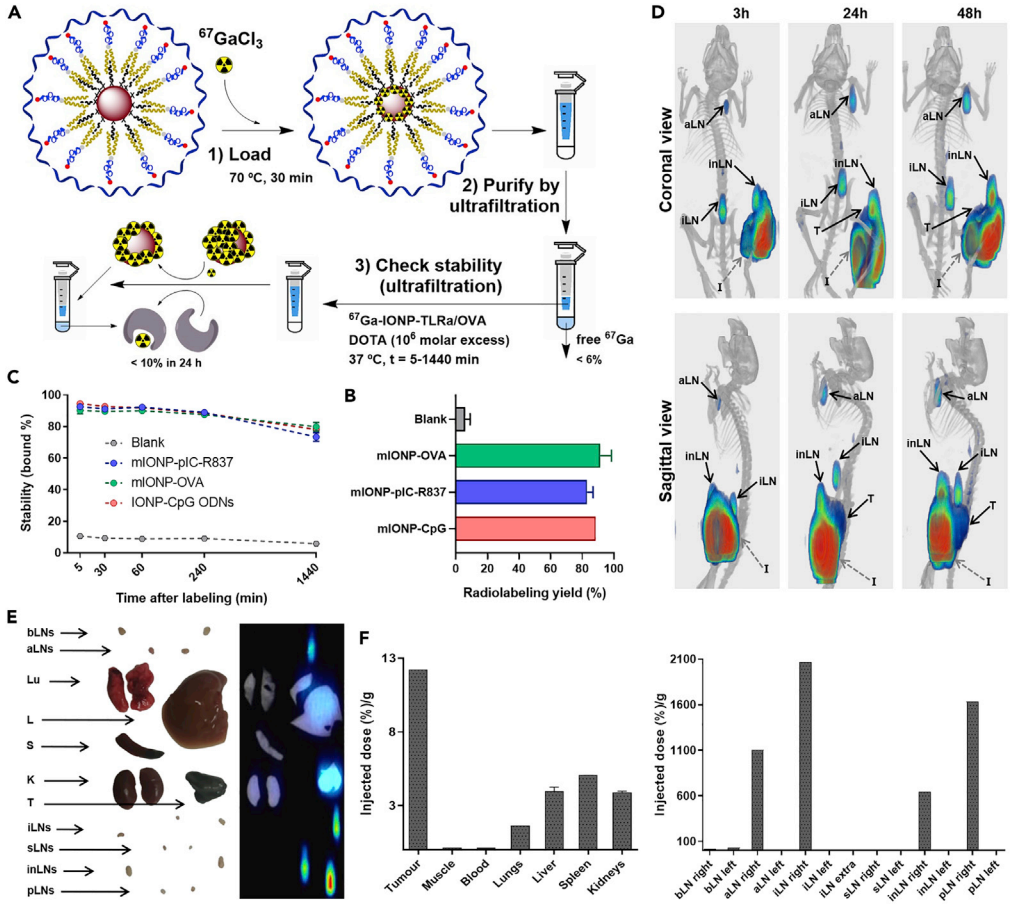

Figure 2. Radiolabeling and SPECT/CT Tracking of IONVs Allow Non-invasive Monitoring of Therapy Outcome

(A and B) The radiocation $[^{67}Ga][Ga(H_2O)_6]Cl_3$(aq.) is loaded by heating with the anionic IONVs and following purification by ultrafiltration using a 100k membrane results in ^{67}Ga-doped IONVs inradiolabeling yields > 80%. (C) The chelator DOTA (present in 10^6 molar excess relative to IONP) is able to remove <10% of the IONP-bound ^{67}Ga over a 24-h period. (D–F) Biodistribution study of ^{67}Ga labeled mIONP-CpG ODNs (23.6 μg of magnetite, 43.4 MBq) injected in the hock of melanoma tumor-bearing mice. (D) SPECT/CT images 3, 24, and 48 h post injection (coronal and sagittal views). *Ex vivo* analysis by (E) SPECT/CT and (F) gamma counter 48 h after injection. T, tumor; bLN, brachial LN; aLN, axillary LN; Lu, lungs; L, liver; S, spleen; K, kidneys; iLN, iliac LN; sLN, sciatic LN; inLN, inguinal LN; pLN, popliteal LN; I, injection site. See also Figures S6 and S7.

significantly slower tumor growth relative to the treatment with free polyIC-R837 and OVA or to the clinical "gold standard" alum or Montanide™ ISA adjuvants. Only the treatment with the IONVs achieved 100% survival through the study endpoint at 30 days after tumor implantation, and the therapeutic effect was elicited with complete absence of systemic toxicity (Figure S8). Notably, the SC administration into the hock of mIONP-OVA without the TLRa adjuvant and even of mIONP alone showed an antitumor effect that is the same or superior to antigen administered intratumorally (IT), highlighting an important intrinsic IONP therapeutic contribution (Figure 3A).

In line with these findings and to investigate whether IONVs promote a long-term immune response involving tumor antigen-specific CTL activation, we conducted prophylactic vaccination experiments. On day 70 after the last immunization, animals were rechallenged with melanoma cells in the contralateral side. Six weeks later, mice were sacrificed and blood and spleens were collected for immune analysis (Figure S9). IONVs were found to enable an enhanced overall specific immune response, resulting in higher percentages of OVA-specific CTLs that exhibited a multifunctional killing phenotype, as demonstrated by the increased frequency of IFN-γ and TNF-α-producing T cells and increased expression of the degranulation molecule CD107a. Moreover, higher levels of antigen-specific Th1-type $CD4^+$ Th cells (producing IFN-γ and TNF-α Th1-type cytokines) and increased

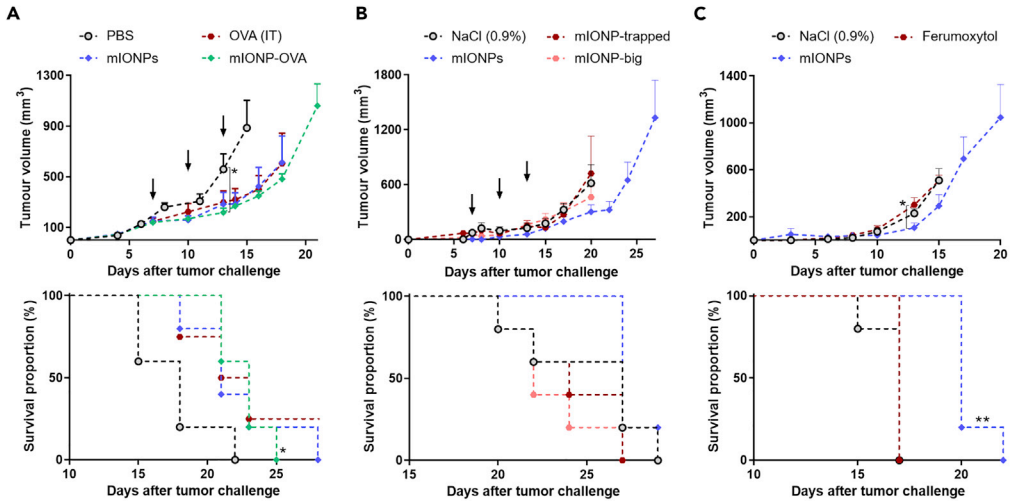

Figure 3. *In Vivo* Evaluation of the Therapeutic Effect Derived from the "Stealth" Hydrophobic IONP Coating and IONP Size

C57BL/6 mice (n = 5) were treated on days 7, 10, and 13 after B16-F10(OVA) cells injection in the right back. (A) intrinsic adjuvant activity of mIONP was analyzed by treating animals with 10 μg of OVA antigen alone (IT) or in combination (as protein corona adsorbed by the nanoparticle) with mIONP (SC injection into the hock [ankle]; 61 μg magnetite); (B) nanoparticle size and exposure of coating was studied by injecting animals with different IONP-filled micelle designs (101 μg magnetite) peritumorally (SC, 2 cm from tumor); and (C) the effect of IONP coating nature was examined by comparing the co-administration (SC, right back) of B16-F10(OVA) cancer cells with IONPs with polar (ferumoxytol) or apolar (mIONP) coating (12 mg Fe/kg, 332 μg magnetite).

(A–C) Results are shown as average tumor growth curves (upper graphs) and Kaplan-Meier survival curves for each case group (lower graphs). Arrows indicate the days of therapy administration. Data are shown as mean ± SEM. *$p < 0.05$, **$p < 0.01$ by two-tailed unpaired Student's t test (A–C upper graphs) and by log rank (Mantel-Cox) test against PBS/NaCl (0.9%) control group (A–C lower graphs).See also Figures S8–S10 for further *in vivo* studies and Figure S2 for characterization of the hydrophobic IONPs.

quality of the T cell response based on the analysis of effector (T_{EM}) and central memory (T_{CM}) $CD8^+$ T cell percentages in spleen were also observed. The characterization of the immune responses confirmed the ability of IONVs to elicit potent and durable antitumor immunity.

To elucidate potential intrinsic adjuvant properties, we assessed the status of DCs after incubation with the designed mIONP alone and IONVs carrying TLRa adjuvants and OVA. The expression of the co-stimulatory signal molecules CD80 and CD86 as well as the major histocompatibility complex (MHC) class II, which are involved in the initiation of T cell-mediated immune responses against tumors, was observed with the mIONP alone and was comparable with the expression induced by stimulation with free TLRa agonists (Figure 4).

This result highlights the importance of the mIONPs toward promoting proper DC maturation for T cell clonal expansion and differentiation to $CD8^+$ cytotoxic lymphocytes (CTLs) and improved co-presentation of antigen to $CD4^+$ T helper (Th) cells. None of the mIONP formulations showed toxicity in DCs. Notably, the induction of the expression of PD-L1, which inhibits T cell effector function (via engagement of the PD-1 receptor expressed on activated T cells), was observed on DCs activated by the TLRa agonists and mIONP formulations (Figures 4 and 5). This result suggests that blocking PD-1/PD-L1 signaling could represent an opportunity to augment the antitumor effects of these systems.

Hydrophobicity as ancient damage associated molecular pattern (DAMP) can be used to activate innate immune responses (Seong and Matzinger, 2004). To investigate if the micellar structure with "stealth" hydrophobic portions around IONPs (hydrophobic oleic acid coating covered by PEG-PL layer) contributes toward delaying tumor growth *in vivo*, mice with established tumors were treated with drug-free mIONPs differing in the amphiphilic organic coating and IONP core. If the concept that nanoparticle-tuned disassembly by amphiphilic polymer release from a mIONP system to reveal hydrophobic portions can be used as an IONV design principle to trigger an improved activation of an innate immune response capable of

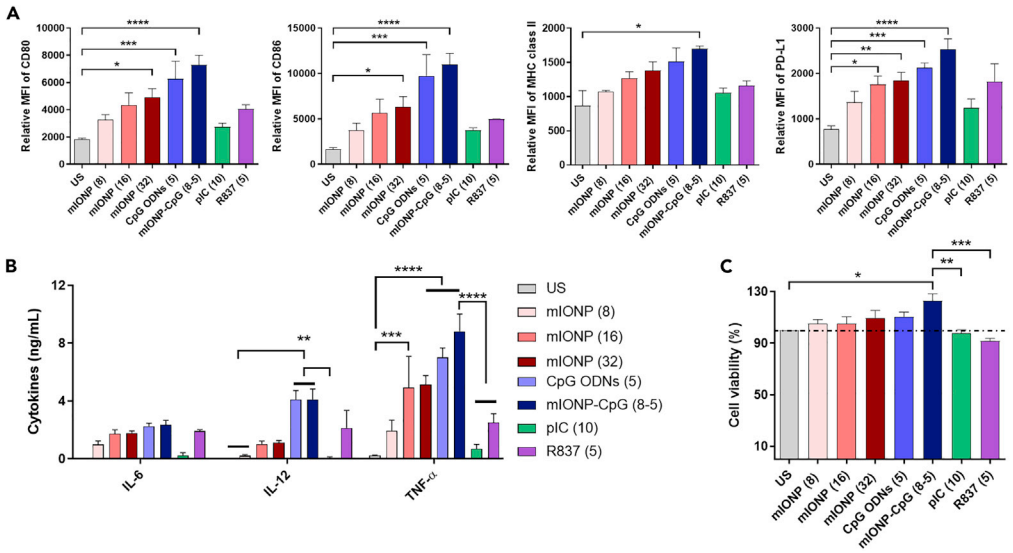

Figure 4. Comparison of DC Activation Elicited by mIONPs and Potent Immunostimulatory TLRa

Primary culture of BMDCs was incubated overnight with increasing concentrations of mIONPs (magnetite μg/mL) and standard amounts of TLR agonists (μg/mL) diluted in media.

(A) Activation and immunosuppressive marker expression measured by flow cytometry and expressed as relative mean fluorescent intensity (MFI).

(B and C) (B) Cytokine production on cell culture supernatant measured by ELISA and (C) cytotoxic effect of the different stimulus after overnight incubation (MTT assay). Results are shown as mean ± SEM of three independent experiments. *p < 0.05, **p < 0.01, ***p < 0.001, ****p < 0.0001 by one-way ANOVA (A and C) and by two-way ANOVA (B) followed by Tukey's test. See also Figure S3 for characterization of mIONPs

influencing tumor immunity and growth is correct, then modulating the stability of the intercalation with the IONP-bound oleates would be expected to affect the extent of tumor growth inhibition. Indeed, the results showed greater inhibition of tumor growth and prolonged survival with administration of mIONP coated with DPPE-mPEG(2000)-PL with methoxy end groups compared with PMAO-PEG as amphiphilic polymer coating (mIONP-trapped) (Figure 3B). This is consistent with the reported high stability of the PMAO-PEG coating (Yu et al., 2006). Using DPPE-mPEG(2000)-IONP micelles containing IONP core sizes of 20 nm (mIONP-big) instead of 6 nm the intrinsic therapy effects were abrogated, which could be derived from an inefficient migration toward TDLNs (Figures 3B and S10).

Administration of the US Food and Drug Administration (FDA)-approved iron supplement ferumoxytol has been found to promote tumor growth regression (Zanganeh et al., 2016). However, when the B16-F10(OVA) melanoma cells were implanted with or without ferumoxytol and compared with an equivalent dose of mIONPs, only the mIONP was able to suppress tumor growth highlighting the superior design features of the mIONPs (Figure 3C).

Antigen Attachment Mode Alters the Efficacy of IONVs

The concept of antigen-specific cancer immunotherapy is based on the generation of antigen-specific CTLs that recognize and destroy tumor cells that present antigen-derived peptides using cell surface MHC class I molecules (Embgenbroich and Burgdorf, 2018). However, many current strategies lead to the ineffective generation of antigen-specific CTLs after vaccination. Our approach to overcome this challenge is based on creating chemically engineered antigen-packed NPs, which can deliver antigen to DCs in the tumor and TDLNs and utilize pathogen-like endocytosis mechanisms. A suitably designed NP can promote the release of antigen in response to intracellular environmental stimuli (e.g., acidic pH) to promote cross-presentation (i.e., presentation of the internalized tumor antigen by means of the MHC-I pathway). Importantly, it has been postulated that lipid peroxidation in DCs can also cause endosomal antigen release for cross-presentation(Dingjan et al., 2016). Our converged solution is to exploit the peroxidative activity of the nanoparticle (*vide infra*) while optimizing NP-enhanced antigen delivery by means of a more efficient antigen chemical attachment mode. We developed a bis-aryl hydrazine linkage strategy for the coupling of

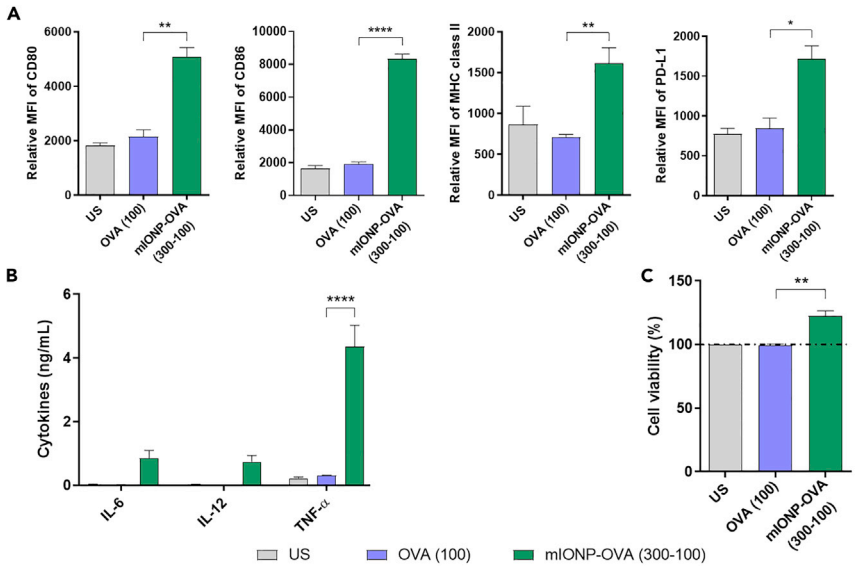

Figure 5. Comparison of DC Activation with mIONP-OVA (Magnetite-Antigen, μg/mL) and OVA

(A–C) (A) Expression of surface markers measured by flow cytometry, (B) cytotoxic effect (MTT assay), and (C) cytokine production measured by ELISA. Results are shown as mean ± SEM of three independent experiments. *$p < 0.05$, **$p < 0.01$, ****$p < 0.0001$ by one-way ANOVA (A and C) and by two-way ANOVA (B) followed by Tukey's test. See Figure S3 for mIONP-OVA characterization.

mIONPs to the tumor antigen, which provides rapid, monitorable, and high yields of conjugation and stability at physiological pH, while enabling antigen release at endosomal pH for efficient cross-presentation (Traini et al., 2019).

To investigate the importance of the new antigen attachment mode, we treated mice with IONVs based on OVA adsorbed to the IONP micelles as a corona (mIONP-OVA(ads)) and its covalent conjugation by hydrazone linkages (mIONP-OVA(hyd)) (Figure 6). Although vaccination with adjuvant mIONP-polyIC-R837 co-administered with mIONP-OVA(ads) or mIONP-OVA(hyd) significantly suppressed tumor growth and the tumors were on average similar in size, only mice in the mIONP-OVA(hyd)-treated group survived tumor-free over a long period of monitoring (CR 40%) (Figure 6C). This result reveals that hydrazone bioconjugation chemistry optimizes therapeutic immune responses to the IONVs.

The Iron Oxide Core Elicits Antitumor Immunotherapy Efficacy

Having established several features that improve the IONV vaccination efficacy, we considered whether other biocompatible nanoparticles previously used for development of nanovaccines such as gold nanoparticles (AuNPs) (Almeida et al., 2014) might elicit similar antitumor efficacy. Studies have highlighted the potential of polyethylenimine (PEI) (Shen et al., 2017; Liang et al., 2018), one of the well-studied cationic polymers used as a transfection reagent for decades, for vaccine development. The mechanisms for the intrinsic immunoactivation function of PEI are diverse and include the triggering of "danger signals" in antigen-presenting cells and the ability to elicit ROS (Shen et al., 2017). We prepared AuNPs coated with PEI (Garaikoetxea Arguinzoniz et al., 2015) and by exploiting its positive charge, we developed PEI-modified AuNPs suitable for forming complexes with the anionic polyIC-R837 adjuvant. Moreover, the AuNPs@PEI-polyIC-R837 complexes had an optimal size for effective lymphatic delivery (Figure S11). Strikingly, the antitumor efficacy of this system was similar to that of mIONP-OVA(hyd) alone. Hence, the AuNP@PEI-polyIC-R837 complex is not able to replicate the adjuvant effects of mIONP-polyIC-R837 (Figure 6) owing to the intrinsic effects arising from the IONP core (see below).

Catalytic Properties and Cell Responses to mIONPs/IONVs: Creating the "Perfect Storm" and Catalytic Therapy

IONPs have been shown to perform peroxidase-like functions, which have led to proof-of-concept demonstrations of tumor-responsive catalytic nanomedicine (Huo et al., 2017; Lin et al., 2018). We reasoned that

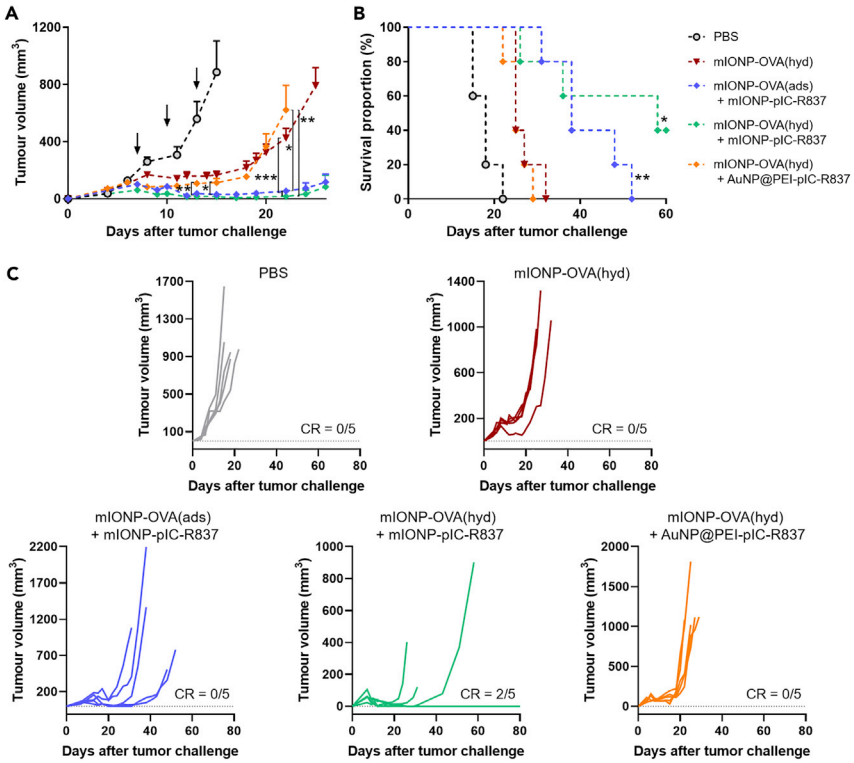

Figure 6. *In Vivo* Evaluation of the Therapeutic Efficacy Arising from an Optimized Antigen Nanoparticle Attachment and Adjuvant Core Material

C57BL/6 mice (n = 5) were treated on days 7, 10, and 13 after 3 × 10^5 B16-F10(OVA) cells injection in the right back with vehicle, 10 μg of OVA adsorbed by IONP (mIONP-OVA(ads)), conjugated to IONP by hydrazone linkages (mIONP-OVA(hyd)) alone or co-administered with adjuvants (mIONP-pIC-R837 or AuNP@PEI-pIC-R837 (4 μg of pIC and 2 μg of R837, 30 μg magnetite, and 5 μg of gold)).

(A–C) (A) Average tumor growth, (B) Kaplan-Meier survival plot, and (C) individual tumor growth curves. CR, complete rejection. Arrows indicate the days of therapy administration. Data are shown as mean ± SEM. *$p < 0.05$, **$p < 0.01$, ***$p < 0.001$ by unpaired Student's t test between indicated groups (A) and by log rank (Mantel-Cox) test against AuNP@PEI-pIC-R837 group (B). See also Figures S3–S5 for IONV characterization, Figure S11 for AuNP@PEI characterization, and Figure S12 for further statistical analysis.

the unique antitumor effectiveness of the IONVs may be underpinned by its catalytic activity on iron and ROS-mediated processes in macrophages and cancer cells.

The peroxidase-like activity of mIONP was assayed by the colorimetric reaction of H_2O_2 with the peroxidase substrate 3,3′,5,5′-tetramethylbenzidine (TMB), which upon oxidation turns blue (ε_{652} = 3.9 × 10^4 M^{-1} cm^{-1}, Figure 7A). mIONP catalyzed the peroxidative reactions at the acidic conditions found in the TME and endosomal compartments to which the nanovaccines are targeted, whereas this activity was minimal at physiological pH. This activity was further confirmed by oxidation of *o*-phenylenediamine (OPD) (Figure 7B). UV-vis absorption time course curves indicated that the mIONPs had a higher catalytic activity than ferumoxytol and AuNPs under the same conditions (Figure 7A). The catalytic contribution of iron ions leached from mIONPs was found to be negligible (Figure 7A), confirming that the peroxidative activity is carried out by the nanoparticles.

Varying the concentration of H_2O_2 and TMB, Michaelis-Menten steady-state kinetics were applied to determine the catalytic performance of the IONP micelles in terms of catalytic rate (k_{cat}), maximal rate (V_{max}), Michaelis constant (K_M), and catalytic efficiency (k_{cat}/K_M) (Figures 7C and 7D). The kinetic parameters (K_M = 0.338 mM, V_{max} = 6.59 × 10^{-8} M^{-1} s^{-1}) are indicative of strong catalytic performance (e.g., better than horseradish peroxidase [HRP] in terms of H_2O_2 affinity, for which the K_M is 3.7 mM). It is known that, during tumor growth, the TME generates a substantial amount of H_2O_2 (~50–100 μM) (Szatrowski and Nathan, 1991), and it is reasonable to expect that this H_2O_2 production will be significantly enhanced by the

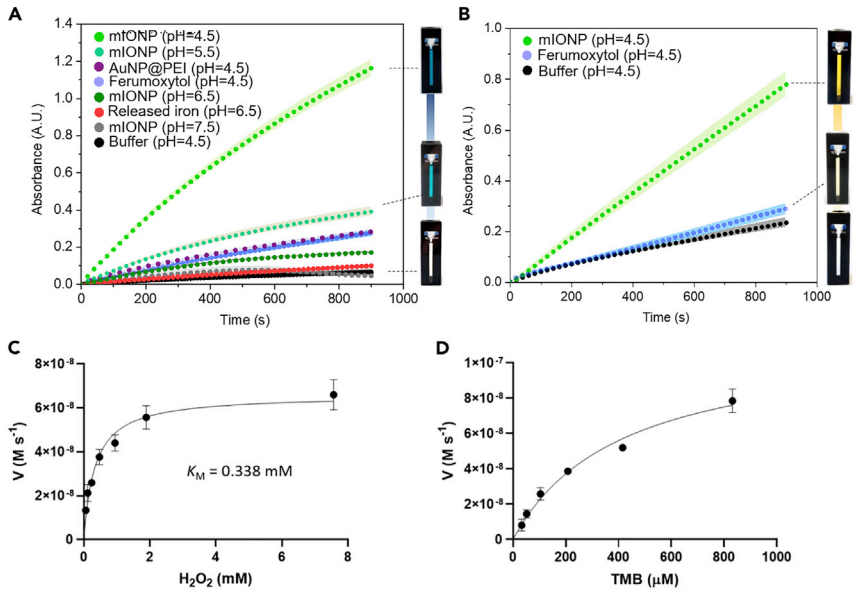

Figure 7. Comparison of Catalytic Properties of mIONPs AuNPs and Ferumoxytol

(A and B) (A) Peroxidase-like activity of mIONPs at different pH values, AuNP@PEI, ferumoxytol, and released free iron cations in catalyzing the oxidation of 3,3′,5,5′-tetramethylbenzidine (TMB). (B) Catalytic oxidation of *o*-phenylenediamine (OPD). Concentrations of [Fe] = 150 μM for mIONPs and 550 μM for ferumoxytol were used.

(C and D) Michaelis-Menten kinetics plots for the oxidation of TMB in the presence of H_2O_2 at varying concentrations of (C) H_2O_2 and (D) TMB, based on data (mean ± SEM) from three independent experiments.

immunostimulatory TLRa-loaded IONVs. The data show that mIONPs catalyze the oxidation of TMB at iron concentration of 150 μM, which is below the concentration used in the *in vivo* and *in vitro* studies.

Tumor-associated macrophages (TAMs) often represent a dominant proportion of the immune cell infiltrate that can promote tumor progression, and suppress antitumor immune responses, but can be potentially harnessed to treat cancer (Bronte and Murray, 2015; Gabrilovich et al., 2012). Having demonstrated high catalytic peroxidative activity, we investigated the effects of mIONP on macrophages and cancer cells in direct cell-to-cell contact co-cultures. For comparison, the cells were also treated with cisplatin, polyIC, and R837. Although the widely used chemotherapy drug is not effective at killing the melanoma cells, it leads to complete macrophage obliteration (Figures 8A and 8B). PolyIC and R837 induced melanoma cell death but only when combined, synergizing to significantly enhance cytotoxicity in the melanoma cells with no toxic effects in macrophages. Free mIONPs were as effective at killing the melanoma cells as the combination of polyIC and R837. Notably, administration of mIONP-polyIC-R837 killed >90% of the target melanoma cells with >70% macrophage viability.

We then performed the studies with both types of cells in mono-cultures and in co-cultures separated by a porous membrane allowing free diffusion treatment and biochemical cell communication while restricting cell migration (Figure S13A). Again, mIONP induced more toxicity in melanoma cells than in macrophages and displayed an overall anticancer effect comparable with the highest dose of cisplatin (100 μM) (Figures 8A, 8B, S13B, and S13C). However, the results clearly highlighted the relevance of cell-to-cell contact interactions between the immune and melanoma cells to potentiate the mIONP immunotherapeutic effect.

We measured the production of IL-10, an effector molecule of M2 macrophages, which as an anti-inflammatory cytokine plays a critical role in limiting the host pro-inflammatory immune response and promoting tumor immune escape. Cultures treated with TLR ligands (including the TLR4 ligand LPS) or cisplatin exhibited high levels of IL-10, whereas treatment with IONP-filled micelles and mIONP-pIC-R837 led to essentially the same level of immunosuppressive IL-10 as the non-treatment control (Figure S13E). Thus, the mIONP-pIC-R837 provides effective melanoma cell killing overcoming mechanisms that impair antitumor immunity.

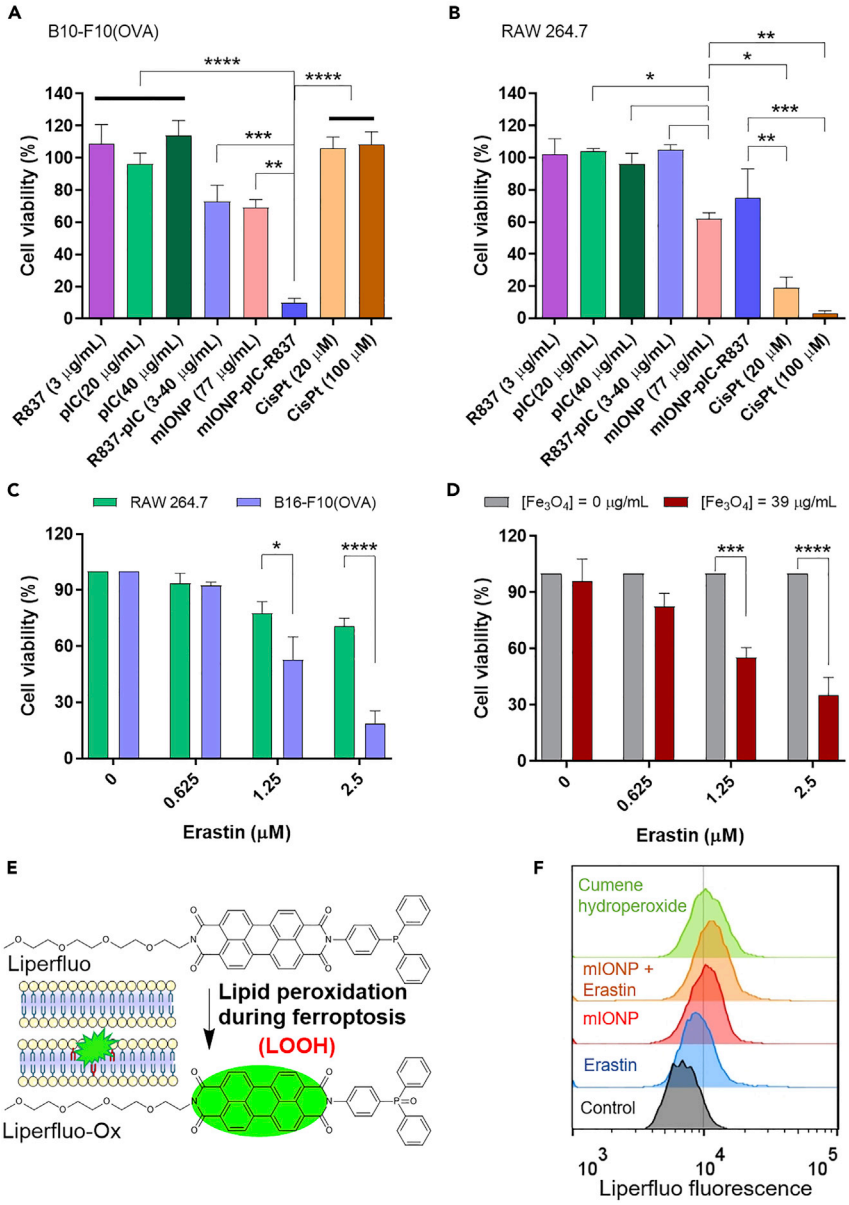

Figure 8. Cell Death Triggered by mIONPs and IONVs in Cell-to-Cell Contact Co-cultures of Melanoma Cells and Macrophages and Induction of Ferroptosis

(A and B) Cell viability was measured by flow cytometry following 24-h treatment (A) B16-F10(OVA) melanoma cells and (B) RAW 264.7 macrophages in cell-to-cell contact co-culture approach (77 μg/mL magnetite = 1 mM of Fe). Data are shown as mean ± SEM (n = 3).

(C) Effects of Erastin on the cell viability of RAW 264.7 (green bars) and B16-F10(OVA) (blue bars) in their respective mono-cultures, after 24 h of exposure determined by MTT assay. Data were normalized to the absence of treatment.

(D) Effects of mIONPs (0.5 mM of Fe) on the cell viability of B16-F10(OVA) after 24 h of exposure upon 24-h preconditioning with increasing concentrations of Erastin. Data were normalized to the absence of mIONP treatment for each Erastin concentration (solid green bars). Data are shown as mean ± SEM (n = 4).

(E) Reaction of Liperfluo with hydroperoxide lipids to generate fluorescence Liperfluo-Ox.

(F) B16-F10(OVA) incubated with IONPs (1 mM of Fe) for 24 h. Representative flow cytometric profiles are shown to demonstrate lipid peroxides with Liperfluo signals, where cells treated with cumene hydroperoxide are used as positive control. *p < 0.05, **p < 0.01, ***p < 0.001, ****p < 0.0001 by one-way ANOVA followed by Tukey's test (A, B) and by two-way ANOVA followed by Sidak's test (C, D). See also Figure S13.

Finally, we sought to identify whether cancer cell death was due to ferroptosis. Using erastin as a ferroptosis activating agent, the results showed that the melanoma cells are much more susceptible to ferroptosis than macrophages (Figure 8C). This result is consistent with other studies showing that cells of the innate immune system display resistance to ferroptosis (Matsushita et al., 2015). Moreover, a recent study has shown that, antitumor M1 macrophages display resistance to ferroptosis, whereas M2 macrophages are sensitive to pro-ferroptosis stimulation and that this is linked to inducible nitric oxide synthase (iNOS)/$NO^{\bullet}$ enrichment (Kapralov et al., 2020).

Importantly, mIONP by providing a source of iron, ROS, and catalytic activity can be used to trigger cancer cell ferroptosis (Figure 8D). Since one of the characteristics of ferroptosis is the accumulation of lipid hydroperoxides, measuring lipid peroxidation is important for evaluating whether ferroptosis occurs. To directly reveal whether lipid hydroperoxides are formed following incubation of the melanoma cells with mIONPs, we used Liperfluo, which reacting with hydroperoxides yields the fluorescent Liperfluo-Ox product (Figure 8E).(Yamanaka et al., 2012) The flow cytometry studies demonstrated the presence of hydroperoxide lipids in melanoma cells treated with mIONP even without erastin (Figure 8F).

Combination Immunotherapy with Checkpoint Inhibitors: "Pushing the Gas" and "Releasing the Brakes"

Immunotherapy with ICIs has created a paradigm shift in clinical oncology. The focus has been blocking inhibitory signals to release the brake on the activity of T cells present in the TME. Recently, several studies reported that this type of immunotherapy leads to production of IFN-γ, which plays a pivotal role in host antitumor immunity (Peng et al., 2012; Chen et al., 2009). However, IFN-γ is a potent inducer of PD-L1 expression and tumors exploit this as a strategy to escape antitumor immunity (Mandai et al., 2016). Importantly, a recent study demonstrates that immunotherapy-activated $CD8^+$ T cells promote tumor cell lipid peroxidation and sensitize tumors to ferroptosis through IFN-γ (Wang et al., 2019). Hence, targeting and enhancing ferroptosis in tumors may be a promising new route to improve the efficacy of cancer immunotherapy (Wang et al., 2019) with additive or potentially synergistic interaction between immunotherapy and induction of ferroptosis. Immunotherapy studies are progressively being directed to immunostimulatory antibodies that instead of releasing the brakes on the immune system to boost antitumor immunity can promote activation pathways (i.e., "step on the gas") (Mahoney et al., 2015). In this context, agonistic anti-OX40 antibodies are being tested in several phase I/II clinical trials either as monotherapy or in combination with other immune-modulating agents. They possess the dual function of enhancing the activation of the tumor infiltrating effector T cells (T_{eff}) and inhibiting the immunosuppressive T_{reg} cells (Aspeslagh et al., 2016). Recent studies have shown that, although systemic delivery of anti-OX40 may favor activation of peripheral lymphocytes to promote systemic toxicity, intratumoral administration is better for targeting tumor-infiltrating lymphocytes and to promote novel mechanisms of action such as depletion of intratumoral T_{reg} and abscopal effects (i.e., a local low-dose immunotherapy eliciting a systemic antitumor immune response avoiding systemic toxic events) (Marabelle et al., 2013; Hebb et al., 2016).

On the basis of these studies and the results shown in this work, we explored combination of the IONVs with an antagonistic anti-PD-L1 (⟨PD-L1) and agonistic anti-OX40 antibodies (⟨OX40).

We first radiolabeled the immunostimulatory mAbs (monoclonal antibodies) with ^{89}Zr by antibody modification with the bifunctional chelator p-isothiocyanatobenthyl-desferrioxamine and addition of [^{89}Zr]Zr-oxalic acid solution (Vosjan et al., 2010). We then confirmed the expression of OX40 and PD-L1 in the TME by ^{89}Zr-immuno-PET imaging and observed high uptake of both radiolabeled antibodies in the tumor and in the spleen (Figures 9A and 9B). The analysis of tumor-infiltrated immune cells by flow cytometry showed high levels of $OX40^+$ T cells in the tumor and TDLNs. Notably, $CD4^+OX40^+$ T cells showed double-positive expression of T cell activation markers CD44 and CD25 (Figures 9C–9E), suggesting an optimal environment for the immunostimulatory mAbs-based therapies.

To study the eradication of established tumors by the combination immunotherapy, mice were treated with IONVs, and, on days 1 and 4 after each vaccination, with ⟨PD-L1 administered (100 μg) intraperitoneally. Although IONVs alone induced delayed growth of the tumor, all animals eventually developed tumor. However, with the combination of vaccination and ⟨PD-L1 treatment in addition to animals showing partial response to the therapy, 40% of mice were free of tumor 90 days after the inoculation of the melanoma cells (Figures 10A–10C). To evaluate whether combination with ⟨OX40 monoclonal antibodies provides

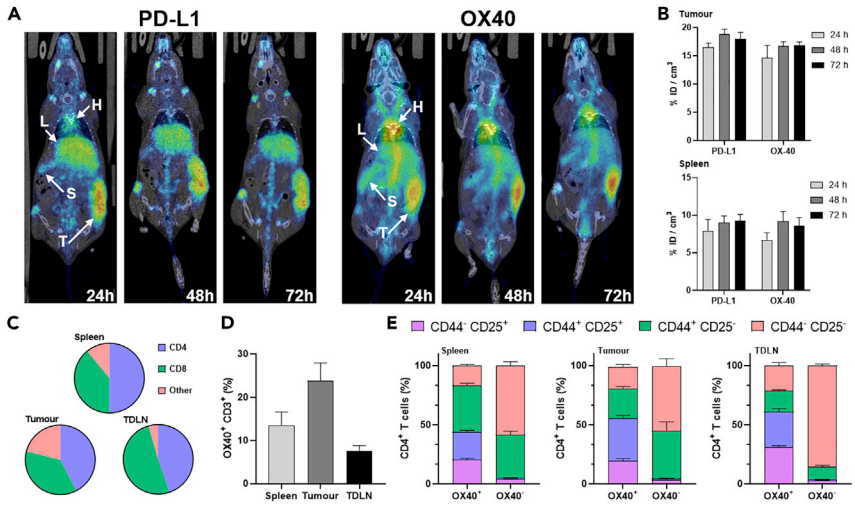

Figure 9. *In Vivo* Detection of the Expression of PD-L1 and OX40 Immune Receptors by Immuno-PET Imaging and Subsequent Analysis of Infiltrating Immune Cells Allowed Characterization of TME Status

(A) PET images were acquired 24, 48, and 72 h after administration of the radiolabeled anti-PD-L1 and anti-OX40 antibodies (80–100 μg, 1–7 MBq).

(B–E) (B) Antibody accumulation in tumor and spleen expressed as injected dose percentage per cm^3 (% ID/cm^3). Analysis of immune cells phenotype found in the spleen, TME and TDLN: (C) $CD4^+$ and $CD8^+$ T cell percentages, (D) $OX40^+$ T cell0020percentages, and (E) activation profile of $CD4^+OX40^+$ T cells. Data are shown as mean ± SEM (n = 7).

additional therapeutic benefit, mice were co-treated with an ultra-low dose of ⟨OX40 antibody (10 μg) delivered intratumorally and the IONVs administered subcutaneously at a tumor distant site. Again, the results consistently show 100% tumor eradication in mice and significantly reduced tumor progression with the combination treatment compared with the monotherapies or checkpoint-inhibition combination therapy with ⟨OX40 and ⟨PD-L1 antibodies (Figures 10A–10C). Moreover, when animals were re-challenged with the melanoma cells (90 days after first tumor challenge) they remained tumor-free for 30 days, compared with none for controls (Figures 10D and 10E).

DISCUSSION

Herein, we report the rationale for a systematic nanoparticle engineering design that exploits the iron content, nanoenzymatic activity, biochemical properties in TME, and chemical and structural features of IONVs as a generalizable therapeutic platform for cancer immunotherapy. A major finding was that iron and peroxidase-like activity of IONVs can be used to exploit and convert conditions in TME (often leading to therapy resistance) into a site that overcomes immunosuppressive mechanisms and elicits potent and durable antitumor responses that eradicate established tumors. The findings show how IONVs can unite and optimize concurrently effective vaccine delivery for inducing anticancer immunity, immune checkpoint blockade, and cancer cell ferroptotic-cell death to augment the therapeutic index of combination therapy and immunotherapy approaches.

Nanoparticles have been extensively studied to improve the delivery of chemotherapy drugs, but the efficacy of this approach has been plagued with disappointing results in clinical trials (Bourzac, 2016; Hare et al., 2017). In contrast, cancer immunotherapy using nanoparticle-based vaccines is a promising new area in which FDA-approved polymers and nanocarriers such as poly(lactic-coglycolic acid) (PLGA), liposomes, and phospholipid nanodiscs have already allowed various degrees of success (Maldonado et al., 2015; Rosalia et al., 2015; Varypataki et al., 2016; Kuai et al., 2017; Min et al., 2017; Xiaoding et al., 2017; Ling et al., 2019). It is becoming clear that nanomedicine can provide innovative solutions for immunotherapy (Irvine and Dane, 2020). Inorganic nanomaterials offer additional features for modulation of immune responses and non-invasive vaccine tracking owing to intrinsic adjuvant and imaging properties (Lee et al., 2012; Cobaleda-siles et al., 2014; Ruiz-De-Angulo et al., 2016; Wang et al., 2016; Bocanegra Gondan et al., 2018). In this study we show that engineered iron oxide nanoparticles (IONPs) can become a cornerstone for enhancing immunotherapy owing to the coupling of catalytic activity with immunomodulation. They are suitable for medical oncology use owing to excellent safety profiles, biodegradability and

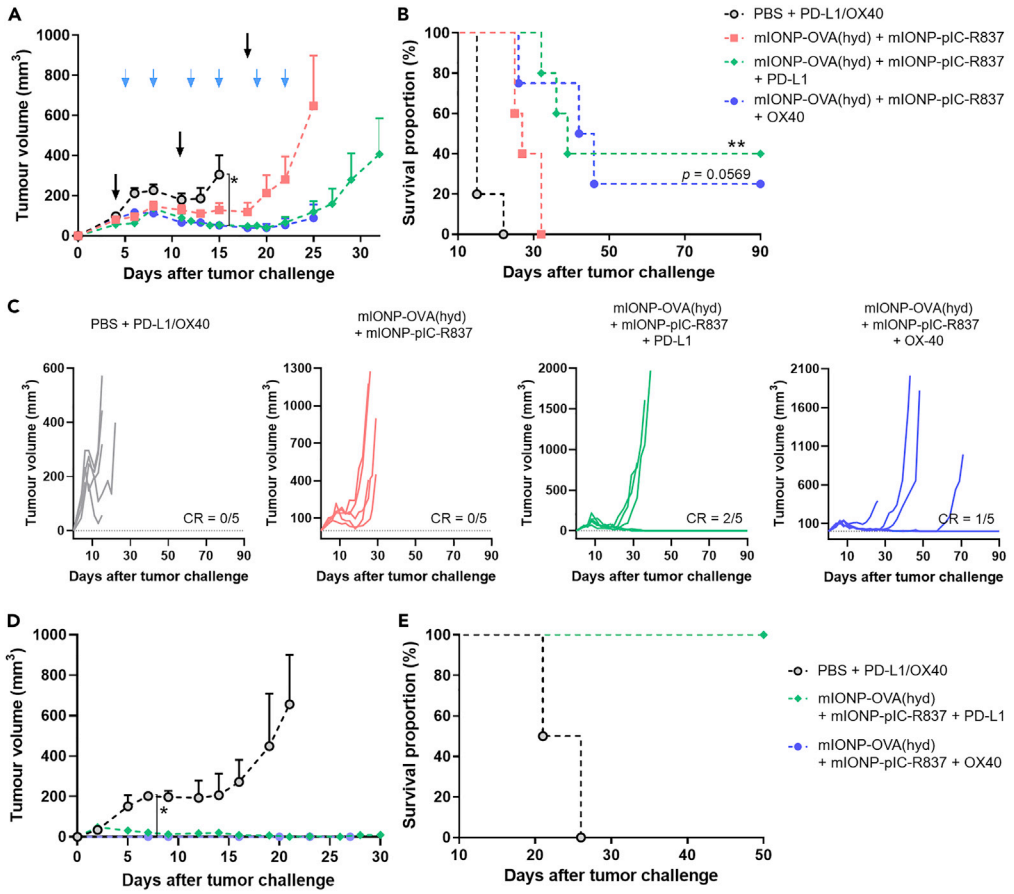

Figure 10. *In Vivo* Evaluation of the Enhanced Effect of Combination Immunotherapy with IONVs and Immunostimulatory mAbs

C57BL/6 mice (n = 5) were inoculated with 3 × 10^5 B16-F10(OVA) cells and treated with nanovaccines (10 μg of OVA, 4 μg of pIC, and 2 μg of R837; 42 μg of magnetite) on days 4, 11, and 18. ICIs (100 μg of anti-PD-L1 (IP) and 10 μg of anti-OX40 (IT)) were administered on days 1 and 4 after each immunization.

(A–E) (A) Average tumor growth, (B) Kaplan-Meier survival plot, and (C) individual tumor growth curves. (D) Average tumor growth and (E) Kaplan-Meier survival plot following re-challenge of melanoma cells in the contralateral back of cured mice. CR, complete rejection. Arrows indicate the days of nanovaccines (black) and checkpoint inhibitors (blue) administration. Data are shown as mean ± SEM. *p < 0.05, **p < 0.01 by unpaired Student's t test between indicated groups (A) and by log rank (Mantel-Cox) test against mIONP-OVA(hyd) + mIONP-pIC-R837 group (B).

metabolization, facile synthesis and tuneability targeting enhancement of intrinsic therapy, and imaging properties (Revia and Zhang, 2016). An important target is to surpass the recently discovered antitumor activities of the FDA-approved IONP-based iron supplement ferumoxytol, which arise from activating and repolarizing macrophages via Fenton chemistry but requires administration of high doses (Zanganeh et al., 2016). Moreover, ferumoxytol administration has been shown to exert anti-leukemic effects exploiting the vulnerability of these cells to iron-based oxidative stress (Trujillo-Alonso et al., 2019). We show how adopting a systematic molecular engineering approach micelles filled with iron oxide nanoparticles can be engineered to significantly surpass the antitumor effects of ferumoxytol.

Consistent with recent studies showing that nanoparticles can induce ferroptosis in cancer cells and perform catalytic nanomedicine (Huo et al., 2017; Kim et al., 2016; Lin et al., 2018; Liu et al., 2018), the mIONP's iron-enabled and high peroxidase-like activity triggered selective cancer cell killing, but in particular in contact co-cultures with macrophages that alone could not induce cancer cell killing.

By targeting ferroptosis (Yang and Stockwell, 2016), which is induced by oxidative stress and characterized by iron-dependent accumulation of lipid hydroperoxides and can be enhanced by the action of immune

checkpoint blockade-reinvigorated T cells (Wang et al., 2019), the IONVs combined with immunostimulatory mAbs can realize complete eradication of aggressive and established melanoma tumors in mice. When benchmarked against other treatments the melanomas proved to be essentially unresponsive to ferumoxytol treatment, adjuvant chemotherapy, vaccination with AuNPs, clinically approved aluminum hydroxide and Montanide-based adjuvants, and a combination of mAbs targeting co-stimulatory and coinhibitory signal in T cells (anti-OX40 and anti-PD-L1).

To target the sites of interest the inherently therapeutic IONVs incorporated a comprehensive and sophisticated delivery mechanism, which involves efficient delivery to TME and lymph nodes, efficient intracellular delivery to DCs by pathogen-mimicking endocytosis, and a chemically engineered conditional intracellular release and antitumor activity that exploits hydrazone bond cleavage and peroxidase-like catalysis in acidic endolysosomes. The radiolabeling of IONVs and ICIs confirmed the mechanistic basis for the combination therapy efficacy by enabling non-invasive monitoring of effective multi-pronged therapy delivery and real-time assessment of expression of blocking and activating immune checkpoint receptors.

Itemizing and evaluating the nanoparticle engineering features hypothesized to contribute to the enhancement of therapeutic outcomes allows a rational and on-demand design of IONVs. As expected, improvements were driven by several characteristics of the designed IONVs: (1) ability to locally deliver the multi-pronged therapeutic cargo to tumor and TDLNs enabled by IONVs size characteristics (<100 nm and spherical IONPs of 6 nm); (2) optimal tumor antigen delivery and cross-presentation through pH-responsive hydrazone conjugation and peroxidase-like activity; (3) nanoparticle-tuned disassembly to activate the "stealth" immunostimulation by the pathogen-mimicking hydrophobic nature of the nanoparticle core, which confers an intrinsic adjuvant activity to the nanosystem; and (4) iron and high catalytic activity of the iron oxide core that allows effective and stable radiolabeling with $^{67/68}$Ga for therapy tracking, reprogramming of macrophages, *in situ* generation of ROS, and further tumor cell sensitization to ferroptosis in the TME.

Although several externally triggered bioengineering approaches such as PTT, PDT, MHT, and magnetic navigation have demonstrated considerable promise for improving treatment outcomes with ICIs (Lucky et al., 2015; Ni et al., 2018; Chao et al., 2019; Eranki et al., 2019), most face challenges for clinical implementation owing to the intrinsic limitations of these techniques. In contrast, use and administration of iron and catalytically enhanced IONVs is easy to implement alongside chemotherapy, radiotherapy, and complementary immunotherapies. The effectiveness of tumor antigen hydrazone bond conjugation is demonstrated with full-length xeno-antigen OVA, yet this chemistry is readily applicable with peptide antigens and neoantigens that could be generated in controlled synthesis or on site (Min et al., 2017; Kuai et al., 2017). This offers a feasibility strategy to eventually achieve personalized treatments, which promises to be the next big immunotherapy and cancer treatment breakthrough.

In conclusion, the results presented here show how chemically programmed IONVs can be used as a platform for the engineering of vaccines that are intrinsically therapeutic exploiting TME reprogramming, and the tumor susceptibility to iron- and ROS-dependent processes and redox stress that could be clinically applicable during combination immunotherapy. Chemistry- and iron-enabled catalytic vaccines offer intriguing opportunities to also invigorate immunotherapy combinations with chemotherapy and radiotherapy and with other approaches such as PDT, PTT, MHT, and HIFU and magnetic navigation.

Limitations of the Study

Although the murine B16 melanoma model is widely used for preclinical assessment of immunotherapies, the therapeutic efficacy of the chemically programmed IONVs in clinically relevant models of human cancer needs to be undertaken. The intracellular mechanism(s) of antigen processing and presentation underpinning cross-presentation is not investigated. The potential role of lipid peroxidation induced by the IONVs also causing endosomal antigen release for cross-presentation is plausible but has not been investigated. Other immune cell populations around TME after the treatment can be investigated to provide a more comprehensive understanding of the IONV effects. How the mIONVs enhance ferroptosis and can be optimized for this purpose and the demonstration of the synergistic induction of ferroptosis by the checkpoint inhibitors will require additional studies.

Resource Availability

Lead Contact

Further information and requests for resources and reagents should be directed to and will be fulfilled by the Lead Contact, Juan C. Mareque-Rivas (juan.mareque-rivas@swansea.ac.uk).

Materials Availability

This study did not generate new unique reagents.

Data and Code Availability

This study did not generate/analyze any datasets/code.

METHODS

All methods can be found in the accompanying Transparent Methods supplemental file.

SUPPLEMENTAL INFORMATION

Supplemental Information can be found online at https://doi.org/10.1016/j.isci.2020.101499.

ACKNOWLEDGMENTS

J.C.M.-R. and J.L. thank MediSURF project (PCIN2016-085) from the Spanish Ministry of Economy and Competitiveness (MINECO). This work was supported by an EPSRC PhD Studentship to M.B.-A. and R.B. (EP/N509553/1 and EP/R51312X/1). J.L. acknowledges financial support from the Spanish Ministry of Economy and Competitiveness (MINECO), grant number CTQ2017-87637-R. The authors would like to thank Dr. Vanessa Gómez-Vallejo and Víctor Salinas for ^{89}Zr production, Zuriñe Baz for assistance in image quantification, April Rees for flow cytometry studies, and Dr. Asís Palazón (bioGUNE) and Dr. Nick Jones (Swansea Medical School) for critically reading the manuscript.

AUTHOR CONTRIBUTIONS

A.R.d.A. prepared and characterized the nanovaccines, performed their radiolabeling, and designed and performed the tumor experiments, SPECT/CT imaging experiments, *in vitro* immune experiments (DCs and CD8$^+$ T cells), and the phenotype analysis of OX40 T cells and contributed to the writing of the manuscript. M.B.-A. prepared and characterized the nanovaccines, performed the catalytic activity assays and the co-culture experiments, and contributed to the writing of the manuscript. J.C.M.-R. oversaw the research project and contributed to planning experiments and interpreting the data and wrote the manuscript. J.L. and I.V.J.F. performed radiolabeling and nuclear imaging studies. K.Z.B. provided valuable technical assistance during the *in vivo* studies. S.J.E and M.J.D.C. supported the *in vitro* cellular assays. J.C and R.B. designed and performed the ferroptosis studies. All authors reviewed the manuscript.

DECLARATION OF INTERESTS

The authors declare no competing interests.

Received: May 6, 2020
Revised: July 24, 2020
Accepted: August 21, 2020
Published: September 25, 2020

REFERENCES

Almeida, J.P.M., Figueroa, E.R., and Drezek, R.A. (2014). Gold nanoparticle mediated cancer immunotherapy. Nanomedicine *10*, 503–514.

Anderson, K.G., Stromnes, I.M., and Greenberg, P.D. (2017). Obstacles posed by the tumor microenvironment to T cell activity: a case for synergistic therapies. Cancer Cell *31*, 311–325.

Aspeslagh, S., Postel-Vinay, S., Rusakiewicz, S., Soria, J.C., Zitvogel, L., Marabelle, A., et al. (2016). Rationale for anti-OX40 cancer immunotherapy. Eur. J. Cancer *52*, 50–66.

Bocanegra Gondan, A.I., Ruiz-de-Angulo, A., Zabaleta, A., Gómez Blanco, N., Cobaleda-Siles, B.M., García-Granda, M.J., Padro, D., Llop, J., Arnaiz, B., Gato, M., et al. (2018). Effective cancer immunotherapy in mice by polyIC-imiquimod complexes and engineered magnetic nanoparticles. Biomaterials *170*, 95–115.

Bourzac, K. (2016). News feature: cancer nanomedicine, reengineered. Proc. Natl. Acad. Sci. U S A *113*, 12600–12603.

Bronte, V., and Murray, P.J. (2015). Understanding local macrophage phenotypes in disease:

modulating macrophage function to treat cancer. Nat. Med. *20*, 117–119.

Carion, O., Mahler, B., Pons, T., and Dubertret, B. (2007). Synthesis, encapsulation, purification and coupling of single quantum dots in phospholipid micelles for their use in cellular and in vivo imaging. Nat. Protoc. *2*, 2383–2390.

Chao, Y., Chen, G., Liang, C., Xu, J., Dong, Z., Han, X., Wang, C., and Liu, Z. (2019). Iron nanoparticles for low-power local magnetic hyperthermia in combination with immune checkpoint blockade for systemic antitumor therapy. Nano Lett. *19*, 4287–4296.

Chen, H., Liakou, C.I., Kamat, A., Pettaway, C., Ward, J.F., Tang, D.N., Sun, J., Jungbluth, A.A., Troncoso, P., Logothetis, C., et al. (2009). Anti-CTLA-4 therapy results in higher CD4+ICOShi T cell frequency and IFN-γ levels in both nonmalignant and malignant prostate tissues. Proc. Natl. Acad. Sci. U S A *106*, 2729.

Chen, L., and Han, X. (2015). 'Anti–PD-1/PD-L1 therapy of human cancer: past, present, and future'. J. Clin. Invest. *125*, 3384–3391.

Chiang, C.S., Lin, Y.J., Lee, R., Lai, Y.H., Cheng, H.W., Hsieh, C.H., Shyu, W.C., and Chen, S.Y. (2018). Combination of fucoidan-based magnetic nanoparticles and immunomodulators enhances tumour-localized immunotherapy. Nat. Nanotechnol. *13*, 746–754.

Cluff, C.W. (2009). Monophosphoryl Lipid A (MPL) as an Adjuvant for Anti-cancer Vaccines: Clinical Results (Springer), pp. 111–123.

Cobaleda-siles, M., Henriksen-Lacey, M., Ruiz de Angulo, A., Bernecker, A., Gómez Vallejo, V., Szczupak, B., Llop, J., Pastor, G., Plaza-Garcia, S., Jauregui-Osoro, M., et al. (2014). An iron oxide nanocarrier for dsRNA to target lymph nodes and strongly activate cells of the immune system. Small *10* (24), 5054–5067.

Dingjan, I., Verboogen, D.R., Paardekooper, L.M., Revelo, N.H., Sittig, S.P., Visser, L.J., Mollard, G.F., Henriet, S.S., Figdor, C.G., Ter Beest, M., et al. (2016). Lipid peroxidation causes endosomal antigen release for cross-presentation. Sci. Rep. *6*, 22064.

Doll, S., Freitas, F.P., Shah, R., Aldrovandi, M., da Silva, M.C., Ingold, I., Goya Grocin, A., Xavier da Silva, T.N., Panzilius, E., Scheel, C.H., et al. (2019). FSP1 is a glutathione-independent ferroptosis suppressor. Nature *575*, 693–698.

Embgenbroich, M., and Burgdorf, S. (2018). Current concepts of antigen cross-presentation. Front. Immunol. *9*, 1643.

Eranki, A., Srinivasan, P., Ries, M., Kim, A., Lazarski, C.A., Rossi, C.T., Khokhlova, T.D., Wilson, E., Knoblach, S.M., Sharma, K.V., et al. (2019). High intensity focused ultrasound (HIFU) triggers immune sensitization of refractory murine neuroblastoma to checkpoint inhibitor therapy. Clin. Cancer Res. *26*, 1152–1161.

Friedman, C.F., Proverbs-Singh, T.A., and Postow, M.A. (2016). Treatment of the immune-related adverse effects of immune checkpoint inhibitors. JAMA Oncol. *2*, 1346.

Gabrilovich, D.I., Ostrand-Rosenberg, S., and Bronte, V. (2012). Coordinated regulation of myeloid cells by tumours. Nat. Rev. Immunol. *12*, 253–268.

Gajewski, T.F., Schreiber, H., and Fu, Y.-X. (2013). Innate and adaptive immune cells in the tumor microenvironment. Nat. Immunol. *14*, 1014–1022.

Galon, J., and Bruni, D. (2019). Approaches to treat immune hot, altered and cold tumours with combination immunotherapies. Nat. Rev. Drug Discov. *18*, 197–218.

Garaikoetxea Arguinzoniz, A., Gómez Blanco, N., Ansorena Legarra, P., and Mareque-Rivas, J.C. (2015). Enhanced cancer cell killing of a Pt(iv) prodrug promoted by outer-sphere coordination with polyethyleneimines. Dalton Trans. *44*, 7135–7138.

Hare, J.I., Lammers, T., Ashford, M.B., Puri, S., Storm, G., and Barry, S.T. (2017). Challenges and strategies in anti-cancer nanomedicine development: an industry perspective. Adv. Drug Deliv. Rev. *108*, 25–38.

Hebb, J.P.O., Mosley, A., Vences Catalan, F., Ellmark, P., Norlen, P., and Felsher, D.W. (2016). Intratumoral administration of the immunotherapeutic combination anti-ctla4, anti-cd137 and anti-ox40: comparison to systemic administration, peri-draining lymph node injection, and cellular vaccine in a mouse lymphoma model. Blood *128*, 4172.

Huo, M., Wang, L., Chen, Y., and Shi, J. (2017). Tumor-selective catalytic nanomedicine by nanocatalyst delivery. Nat. Commun. *8*, 357.

Irvine, D.J., and Dane, E.L. (2020). Enhancing cancer immunotherapy with nanomedicine. Nat. Rev. Immunol. *20*, 321–334.

Irvine, D.J., Swartz, M.A., and Szeto, G.L. (2013). Engineering synthetic vaccines using cues from natural immunity. Nat. Mater. *12*, 978–990.

Jenkins, R.W., Barbie, D.A., and Flaherty, K.T. (2018). Mechanisms of resistance to immune checkpoint inhibitors. Br. J. Cancer *118*, 9–16.

Kang, T.H., Mao, C.P., Lee, S.Y., Chen, A., Lee, J.H., Kim, T.W., Alvarez, R.D., Roden, R.B., Pardoll, D., Hung, C.F., et al. (2013). Chemotherapy acts as an adjuvant to convert the tumor microenvironment into a highly permissive state for vaccination-induced antitumor immunity. Cancer Res. *73*, 2493–2504.

Kapralov, A.A., Yang, Q., Dar, H.H., Tyurina, Y.Y., Anthonymuthu, T.S., Kim, R., St Croix, C.M., Mikulska-Ruminska, K., Liu, B., Shrivastava, I.H., et al. (2020). Redox lipid reprogramming commands susceptibility of macrophages and microglia to ferroptotic death. Nat. Chem. Biol. *16*, 278–290.

Kim, S.E., Zhang, L., Ma, K., Riegman, M., Chen, F., Ingold, I., Conrad, M., Turker, M.Z., Gao, M., Jiang, X., et al. (2016). Ultrasmall nanoparticles induce ferroptosis in nutrient-deprived cancer cells and suppress tumour growth. Nat. Nanotechnol. *11*, 977–985.

Kuai, R., Ochyl, L.J., Bahjat, K.S., Schwendeman, A., and Moon, J.J. (2017). Designer vaccine nanodiscs for personalized cancer immunotherapy. Nat. Mater. *16*, 489–498.

Lee, I.-H., Kwon, H.K., An, S., Kim, D., Kim, S., Yu, M.K., Lee, J.H., Lee, T.S., Im, S.H., and Jon, S. (2012). Imageable antigen-presenting gold nanoparticle vaccines for effective cancer immunotherapy in vivo. Angew. Chem. Int. Ed. *51*, 8800–8805.

Li, C.-X., Dong, Y., Zhang, L., Liu, M.-D., and Zhang. (2019). Artificially Reprogrammed Macrophages as Tumor-Tropic Immunosuppression-Resistant Biologics to Realize Therapeutics Production and Immune Activation. Adv. Mater. *31*, 1807211.

Liang, X., Duan, J., Li, X., Zhu, X., Chen, Y., Wang, X., Sun, H., Kong, D., Li, C., and Yang, J. (2018). Improved vaccine-induced immune responses *via* a ROS-triggered nanoparticle-based antigen delivery system. Nanoscale *10*, 9489–9503.

Lin, H., Chen, Y., and Shi, J. (2018). Nanoparticle-triggered *in situ* catalytic chemical reactions for tumour-specific therapy. Chem. Soc. Rev. *47*, 1938–1958.

Ling, X., Tu, J., Wang, J., Shajii, A., Kong, N., Feng, C., Zhang, Y., Yu, M., Xie, T., Bharwani, Z., et al. (2019). Glutathione-responsive prodrug nanoparticles for effective drug delivery and cancer therapy. ACS Nano *13*, 357–370.

Liu, Y., Naha, P.C., Hwang, G., Kim, D., Huang, Y., Simon-Soro, A., Jung, H.I., Ren, Z., Li, Y., Gubara, S., et al. (2018). Topical ferumoxytol nanoparticles disrupt biofilms and prevent tooth decay in vivo via intrinsic catalytic activity. Nat. Commun. *9*, 2920.

Lucky, S.S., Soo, K.C., and Zhang, Y. (2015). Nanoparticles in photodynamic therapy. Chem. Rev. *115*, 1990–2042.

Mahoney, K.M., Rennert, P.D., and Freeman, G.J. (2015). Combination cancer immunotherapy and new immunomodulatory targets. Nat. Rev. Drug Discov. *14*, 561–584.

Maldonado, R.A., LaMothe, R.A., Ferrari, J.D., Zhang, A.H., Rossi, R.J., Kolte, P.N., Griset, A.P., O'Neil, C., Altreuter, D.H., Browning, E., Johnston, L., et al. (2015). Polymeric synthetic nanoparticles for the induction of antigen-specific immunological tolerance. Proc. Natl. Acad. Sci. U S A *112*, E156–E165.

Mandai, M., Hamanishi, J., Abiko, K., Matsumura, N., Baba, T., and Konishi, I. (2016). Dual faces of IFN in cancer progression: a role of PD-L1 induction in the determination of pro- and antitumor immunity. Clin. Cancer Res. *22*, 2329–2334.

Marabelle, A., Kohrt, H., Sagiv-Barfi, I., Ajami, B., Axtell, R.C., Zhou, G., Rajapaksa, R., Green, M.R., Torchia, J., Brody, J., et al. (2013). Depleting tumor-specific Tregs at a single site eradicates disseminated tumors. J. Clin. Invest. *123*, 2447–2463.

Matsushita, M., Freigang, S., Schneider, C., Conrad, M., Bornkamm, G.W., and Kopf, M. (2015). T cell lipid peroxidation induces ferroptosis and prevents immunity to infection. J. Exp. Med. *212*, 555–568.

Messenheimer, D.J., Jensen, S.M., Afentoulis, M.E., Wegmann, K.W., Feng, Z., Friedman, D.J., Gough, M.J., Urba, W.J., and Fox, B.A. (2017). Timing of PD-1 blockade is critical to effective

combination immunotherapy with anti-OX40. Clin. Cancer Res. *23*, 6165–6177.

Min, Y., Roche, K.C., Tian, S., Eblan, M.J., McKinnon, K.P., Caster, J.M., Chai, S., Herring, L.E., Zhang, L., Zhang, T., et al. (2017). Antigen-capturing nanoparticles improve the abscopal effect and cancer immunotherapy. Nat. Nanotechnol. *12*, 877–882.

Moslehi, J.J., Salem, J.E., Sosman, J.A., Lebrun-Vignes, B., and Johnson, D.B. (2018). Increased reporting of fatal immune checkpoint inhibitor-associated myocarditis. Lancet *391*, 933.

Nguyen, V.H., and Lee, B.J. (2017). Protein corona: a new approach for nanomedicine design. Int. J. Nanomedicine *12*, 3137–3151.

Ni, K., Lan, G., Chan, C., Quigley, B., Lu, K., Aung, T., Guo, N., La Riviere, P., Weichselbaum, R.R., and Lin, W. (2018). Nanoscale metal-organic frameworks enhance radiotherapy to potentiate checkpoint blockade immunotherapy. Nat. Commun. *9*, 2351.

Peng, W., Liu, C., Xu, C., Lou, Y., Chen, J., Yang, Y., Yagita, H., Overwijk, W.W., Lizée, G., Radvanyi, L., et al. (2012). PD-1 blockade enhances T-cell migration to tumors by elevating IFN-γ inducible chemokines. Cancer Res. *72*, 5209–5218.

Pitt, J.M., Marabelle, A., Eggermont, A., Soria, J.C., Kroemer, G., and Zitvogel, L. (2016). Targeting the tumor microenvironment: removing obstruction to anticancer immune responses and immunotherapy. Ann. Oncol. *27*, 1482–1492.

Revia, R.A., and Zhang, M. (2016). Magnetite nanoparticles for cancer diagnosis, treatment, and treatment monitoring: recent advances. Mater. Today *19*, 157–168.

Riley, R.S., June, C.H., Langer, R., and Mitchell, M.J. (2019). Delivery technologies for cancer immunotherapy. Nat. Rev. Drug Discov. *18*, 175–196.

Rosalia, R.A., Cruz, L.J., van Duikeren, S., Tromp, A.T., Silva, A.L., Jiskoot, W., de Gruijl, T., Löwik, C., Oostendorp, J., van der Burg, S.H., et al. (2015). CD40-targeted dendritic cell delivery of PLGA-nanoparticle vaccines induce potent anti-tumor responses. Biomaterials *40*, 88–97.

Ruiz-De-Angulo, A., Zabaleta, A., Gómez-Vallejo, V., Llop, J., and Mareque-Rivas, J.C. (2016). Microdosed lipid-coated ^{67}Ga-magnetite enhances antigen-specific immunity by image tracked delivery of antigen and cpg to lymph nodes. ACS Nano *10*, 1602–1618.

Schmidt, C. (2006). Immune system's toll-like receptors have good opportunity for cancer treatment. J. Natl. Cancer Inst. *98*, 574–575.

Schudel, A., Francis, D.M., and Thomas, S.N. (2019). Material design for lymph node drug delivery. Nat. Rev. Mater. *4*, 415–428.

Seong, S.Y., and Matzinger, P. (2004). Hydrophobicity: an ancient damage-associated molecular pattern that initiates innate immune responses. Nat. Rev. Immunol. *4*, 469–478.

Shapiro, B., Kulkarni, S., Nacev, A., Muro, S., Stepanov, P.Y., and Weinberg, I.N. (2015). Open challenges in magnetic drug targeting. Wiley Interdiscip. Rev. Nanomed. Nanobiotechnol. *7*, 446–457.

Shen, C., Li, J., Zhang, Y., Li, Y., Shen, G., Zhu, J., and Tao, J. (2017). Polyethylenimine-based micro/nanoparticles as vaccine adjuvants. Int. J. nanomedicine *12*, 5443–5460.

Shiao, S.L., Ganesan, A.P., Rugo, H.S., and Coussens, L.M. (2011). Immune microenvironments in solid tumors: new targets for therapy. Genes Dev. *25*, 2559–2572.

Shields, B.D., Mahmoud, F., Taylor, E.M., Byrum, S.D., Sengupta, D., Koss, B., Baldini, G., Ransom, S., Cline, K., Mackintosh, S.G., et al. (2017). Indicators of responsiveness to immune checkpoint inhibitors. Sci. Rep. *7*, 807.

Storni, T., Kündig, T.M., Senti, G., and Johansen, P. (2005). Immunity in response to particulate antigen-delivery systems. Adv. Drug Deliv. Rev. *57*, 333–355.

Szatrowski, T.P., and Nathan, C.F. (1991). Production of large amounts of hydrogen peroxide by human tumor cells. Cancer Res. *51*, 794–798.

Traini, G., Ruiz-de-Angulo, A., Blanco-Canosa, J.B., Zamacola Bascarán, K., Molinaro, A., Silipo, A., Escors, D., and Mareque-Rivas, J.C. (2019). Cancer immunotherapy of TLR4 agonist-antigen constructs enhanced with pathogen-mimicking magnetite nanoparticles and checkpoint blockade of PD-L1. Small *15*, 1803993.

Trujillo-Alonso, V., Pratt, E.C., Zong, H., Lara-Martinez, A., Kaittanis, C., Rabie, M.O., Longo, V., Becker, M.W., Roboz, G.J., Grimm, J., and Guzman, M.L. (2019). FDA-approved ferumoxytol displays anti-leukaemia efficacy against cells with low ferroportin levels. Nat. Nanotechnol. *14*, 616–622.

Varypataki, E.M., Silva, A.L., Barnier-Quer, C., Collin, N., Ossendorp, F., and Jiskoot, W. (2016). Synthetic long peptide-based vaccine formulations for induction of cell mediated immunity: a comparative study of cationic liposomes and PLGA nanoparticles. J. Control. Release *226*, 98–106.

Vosjan, M.J.W.D., Perk, L.R., Visser, G.W., Budde, M., Jurek, P., Kiefer, G.E., and van Dongen, G.A. (2010). Conjugation and radiolabeling of monoclonal antibodies with zirconium-89 for PET imaging using the bifunctional chelate p-isothiocyanatobenzyl-desferrioxamine. Nat. Protoc. *5*, 739–743.

Wang, W., Green, M., Choi, J.E., Gijón, M., Kennedy, P.D., Johnson, J.K., Liao, P., Lang, X., Kryczek, I., Sell, A., et al. (2019). CD8+ T cells regulate tumour ferroptosis during cancer immunotherapy. Nature *569*, 270–274.

Wang, X., Li, X., Ito, A., Watanabe, Y., Sogo, Y., Tsuji, N.M., and Ohno, T. (2016). Stimulation of in vivo antitumor immunity with hollow mesoporous silica nanospheres. Angew. Chem. Int. Ed. *55*, 1899–1903.

Ward, P., S, and Thompson, C., B (2012). Metabolic Reprogramming: A Cancer Hallmark Even Warburg Did Not Anticipate. Cancer Cell *21*, 297–308.

Wei, S.C., Duffy, C.R., and Allison, J.P. (2018). Fundamental mechanisms of immune checkpoint blockade therapy. Cancer Discov. *8*, 1069–1086.

Xiaoding, X., Saw, P.E., Tao, W., Li, Y., Ji, X., Yu, M., Mahmoudi, M., Rasmussen, J., Ayyash, D., Zhou, Y., et al. (2017). Tumor microenvironment-responsive multistaged nanoplatform for systemic RNAi and cancer therapy. Nano Lett. *17*, 4427–4435.

Yamanaka, K., Saito, Y., Sakiyama, J., Ohuchi, Y., Oseto, F., and Noguchi, N. (2012). A novel fluorescent probe with high sensitivity and selective detection of lipid hydroperoxides in cells. RSC Adv. *2*, 7894–7900.

Yang, W.S., and Stockwell, B.R. (2016). Ferroptosis: death by lipid peroxidation. Trends Cell Biol. *26*, 165–176.

Yu, W.W., Chang, E., Sayes, C.M., Drezek, R., and Colvin, V.L. (2006). Aqueous dispersion of monodisperse magnetic iron oxide nanocrystals through phase transfer. Nanotechnology *17*, 4483–4487.

Zanganeh, S., Hutter, G., Spitler, R., Lenkov, O., Mahmoudi, M., Shaw, A., Pajarinen, J.S., Nejadnik, H., Goodman, S., Moseley, M., Coussens, L.M., et al. (2016). Iron oxide nanoparticles inhibit tumour growth by inducing pro-inflammatory macrophage polarization in tumour tissues. Nat. Nanotechnol. *11*, 986–994.

iScience, Volume *23*

Supplemental Information

Chemically Programmed Vaccines: Iron Catalysis in Nanoparticles Enhances Combination Immunotherapy and Immunotherapy-Promoted Tumor Ferroptosis

Ane Ruiz-de-Angulo, Marc Bilbao-Asensio, James Cronin, Stephen J. Evans, Martin J.D. Clift, Jordi Llop, Irene V.J. Feiner, Rhiannon Beadman, Kepa Zamacola Bascarán, and Juan C. Mareque-Rivas

SUPPLEMENTAL INFORMATION

Chemically programmed vaccines: Iron catalysis in nanoparticles enhances combination immunotherapy and immunotherapy-promoted tumour ferroptosis

Ane Ruiz-de-Angulo,[3,*] Marc Bilbao-Asensio,[1] James Cronin,[4] Stephen J. Evans,[4] Martin J. D. Clift,[4] Jordi Llop,[2] Irene V. J. Feiner,[2] Rhiannon Beadman,[4] Kepa Zamacola Bascarán,[2] and Juan C. Mareque-Rivas[1,**]

[1]Department of Chemistry and Centre for NanoHealth, Swansea University, Singleton Park, Swansea, SA2 8PP, UK
[2]Radiochemistry and Nuclear Imaging Laboratory, CIC biomaGUNE, Paseo Miramón 182, San Sebastián, 20014, Spain
[3]Chemical Immunology Laboratory, CIC bioGUNE, Building 801A, Derio, 48160, Spain
[4]Swansea University Medical School, Institute of Life Science, Singleton Park, Swansea SA2 8PP, UK
[*]Correspondence: aruizdeangulo@cicbiogune.es
[**]Correspondence: Lead contact. juan.mareque-rivas@swansea.ac.uk

Transparent methods

Materials

All commercially available reagents were used without further purification.

Synthesis of hydrophobic IONPs: Hexane (99%; LABSCAN), chloroform (water 0.005%; LABSCAN), diphenyl ether (99%; Sigma Aldrich), dibenzyl ether (>98%; Alfa Aesar), 1,2-hexadecanediol (>98%; Tokyo Chemical Industry Co. Ltd), oleic acid (90%; Alfa Aesar), oleylamine (70%; Sigma Aldrich), iron(III) acetylacetonate (99%; Strem Chemicals). *IONP-filled micelles synthesis (mIONPs):* 1,2-dipalmitoyl-sn-glycero-3-phosphoethanolamine-N-[methoxy(polyethylene glycol)-2000] (ammonium salt) (DPPE-mPEG(2000)), 1,2-distearoyl-sn-glycero-3-phosphoethanolamine-N-[carboxy(polyethylene glycol)-2000] (ammonium salt) (DSPE-cPEG(2000)), 1,2-distearoyl-sn-glycero-3-phosphoethanolamine-N-[amino(polyethylene glycol)-2000] (ammonium salt) (DSPE-aPEG(2000)), 1,2-dipalmitoyl-3-trimethylammonium-propane (chloride salt) (DOTAP) lipids were purchased from Avanti Polar Lipids, Inc. *Synthesis of IONVs:* polyIC, CpG ODNs and R837 TLRas were purchased from InvivoGen. Endotoxin-free ovalbumin was obtained from Hyglos GmbH. Succinimidyl 6-hydrazinonicotinamide acetone hydrazone was purchased from Solulink and succinimidyl 4-Formylbenzoate was purchased from Santa Cruz biotechnology. 2-Hydrazinopyridine-2HCl was purchased from Fluorochem. PD MiniTrap G-10 desalting columns were obtained from GE Healthcare and Amicon ultra-0.5 mL centrifugal filters (100 KDa MWCO) and Amicon Ultra-4mL (10 KDa MWCO) were purchased from Merck. *Radiolabeling studies:* ^{67}Ga citrate solution was purchased from Curium™ (Spain) and 1,4,7,10-tetraazacyclododecane-1,4,7,10-tetraacetic acid (DOTA) from Macrocyclics (Inc. Dallas, USA). In vitro *and* in vivo *experiments:* Dulbecco's Modified Eagle Medium (DMEM), RPMI-1640 medium, fetal bovine serum (FBS), Penicillin/Streptomycin (P/S, 50 U/mL) and L-glutamine (200 mM) (all of them from Gibco®) were purchased from Life Technologies (Thermo Fisher Scientific). MTT cell proliferation kit was, Collagenase D and DNase were purchased from Roche and the red blood cells (RBC) lysing buffer and Cytofix/Cytoperm™ Plus Fixation/Permeabilization Kit from BD Biosciences. Granulocyte-macrophage colony-stimulating factor (GM-CSF) was purchased from Peprotech. IL-6 ELISA kit was purchased from R&D, IL-12 and TNF-α ELISA kits from Peprotech and IL-10 ELISA kits from BioLegend. All fluorescently labeled antibodies were obtained from BioLegend, unless specified otherwise. The Fc blocking antibody was purchased from BD Biosciences and bovine serum albumin (≥ 98%, BSA) from Sigma Aldrich. SIINFEKL OVA peptide was obtained from Peptides International and Matrigel® Matrix from Corning. Imject® Alum (Thermo Scientific) and Montanide™ ISA (kindly provided by Seppic) were prepared and used as described in their respective data sheets. B16-F10(OVA) melanoma cell line was a gift from Dr Pablo Sarobe (Centre for Applied Medical Research (CIMA), University of Navarra).

Synthesis and characterisation of nanovaccines

Hydrophobic iron oxide nanoparticles were synthetized following previously described method (Sun *et al.*, 2004; Gomez Blanco *et al.*, 2012). The IONP-filled micelles (mIONPs) were produced by self-assembly using a dry-film hydration method (Carion *et al.*, 2007). Different IONP- to-lipid ratios were used to optimize particle size and formation yield for each kind of PEG-phospholipid. Typically, IONPs (1 mg) were dissolved in chloroform (500 µL) with either DSPE- PEG(2000)-COOH (2 mg), DSPE- PEG(2000)-MAL NH_2 (2.5 mg) / or DPPE-PEG(2000)-OMe (2 mg) plus DOTAP (0.5 mg) (Avanti Lipids). The solvent was left to evaporate overnight at room temperature. Any remaining solvent was removed by placing the dried film under vacuum for 1 hour. The film was finally heated for 30 seconds at

80° C and hydrated by adding 1mL of nanopure water. To maximize the yield of product formation, IONPs combined with DPPE-PEG(2000)-OMe and DOTAP were left to hydrate at room temperature for 2 hours (vortexing gently every 20 minutes), prior to purification. The suspension was purified by centrifugation (1 cycle, 10.000 × g for 5 min), after which the pellet was discarded, and the supernatant was passed through a 0.45 μm PTFE syringe-filter. Any remaining empty micelles were removed by ultracentrifugation (3 cycles, 160.000 g for 50 min) by discarding the supernatant. The synthesis of IONPs stabilised with poly(maleic anhydride-alt-1-octadecene) (PMAO) was carried out as reported previously (Moros *et al.*, 2010).

In the case of the gold nanoparticles, the one-pot synthesis of PEI-modified AuNPs was carried out by mixing a water solution of 1.8 kDa PEI with $HAuCl_4$ in a 2:1 molar ratio and constant stirring at 90° C (Song *et al.*, 2010; Garaikoetxea Arguinzoniz *et al.*, 2015). The reaction was monitored by UV-vis over 2 h and the formation of AuNPs@PEI was confirmed by the appearance of a characteristic localised surface plasmon resonance band at 521 nm. Then, AuNPs@PEI were purified by ultrafiltration using an Amicon Ultra-4 filter device (MWCO 50 kDa).

Model antigen OVA and TLR agonists were attached employing optimized PEG(2000)-phospholipid combinations and ratios and chemistry according to their specific molecular features as described previously (Ruiz-de-Angulo *et al.*, 2016). In the case of model antigen OVA it was incorporated into mIONPs following two different strategies: (i) by mixing the mIONP (1:1 mass ratio of DPPE-mPEG(2000) and DSPE-cPEG(2000)) and the antigen exploiting the concept of 'nanoparticle-protein corona'(Ruiz-de-Angulo *et al.*, 2016), simply allowing the OVA protein to adsorb onto the carrier surface (IONP-OVA(abs)); or employing IONP micelles prepared with 2 mg of DSPE-aPEG(2000) and following a new covalent attachment strategy we described previously (IONP-OVA(hyd)) (Traini *et al.*, 2019). In both cases, unbound OVA was removed by three cycles of ultracentrifugation (1844 × *g* for 5 min) using a NanoSep centrifugal device (Pall Life Sciences, MWCO 100 kDa) and the final amount of bound protein was quantified performing a bicinchoninic acid (BCA) protein assay (Thermo scientific) after absorbance subtraction of the same concentration of parent IONP micelles. To attach the nucleic acid-based TLR agonists, cationic IONP micelles were synthetized using 2 mg of DPPE-mPEG(2000) and 1 mg of cationic phospholipid DOTAP for the negatively charged CpG ODNs (Ruiz-de-Angulo *et al.*, 2016), and polyIC and R867 complex (Bocanegra Gondan *et al.*, 2018). An aliquot of NP stock solution (2 μM of magnetite (*ca.* 10 mM Fe) or 90 nM of AuNPs (*ca.* 3 mM Au)) were mixed with the nucleic acid-based TLR agonists diluted in HyClone water and allowed to self-assemble overnight under slight stirring at room temperature (RT). Next, TLRa ligand excess was removed by three cycles of ultrafiltration (1844 × *g* for 5 min) through a NanoSep centrifugal device (MWCO 100 kDa) and final samples resuspended in desired water volume and stored at 4° C until use. In order to quantify the number of bound ligands, an aliquot of IONP-TLRa of stock solution was digested overnight with 0.2 M NaOH in order to hydrolyze the NPs, which were removed then by ultracentrifugation (369 000 × g, 40 min) to obtain a solution of free TLR ligands. UV−vis absorbance of this solution (λ = 260 nm for nucleic acid-based TLRa and λ = 320 nm for imiquimod) was then converted to concentration by comparison to a standard curve. For AuNP@PEI-pIC-R837 micelles, no further purification was done after TLRa addition, assuming that at the high AuNP@PEI:pIC-R837 ratio used 100 % of the immunostimulatory material was incorporated into the nanocarrier (Thomas and Klibanov, 2003).

For the transmission electron microscopy (TEM; JEOL JEM-2011 microscope operating at 200 kV) images, samples were prepared by depositing a drop of IONP/mIONPs solution (*ca.*

0.5 mg/mL, 2 µL) onto a copper specimen grid coated with a holey carbon film and allowing it to dry. In the case of IONP-filled micelles, TEM grids were polarized using a Quorum technologies K100X glow discharge system. For IONP size determination using TEM, a minimum of 300 particles were measured using the Image J software. High-resolution X-ray photoelectron spectroscopy (XPS) measurements were carried out on Fe 2p and Fe 3p regions of the Fe_3O_4 nanoparticles to determine and confirm their elemental composition and iron content was measured by inductively coupled plasma atomic emission spectroscopy (ICP-AES). Hydrodynamic diameter and zeta-potential of water soluble micelles were characterized with a NanoSizer (Malvern Nano-Zs, UK) with 173° scattering angle at 25° C for size measurement and at 25° C with a cell drive voltage of 25 V (Smoluchowski model) in the case of zeta potential measurements. The results are shown as a mean of at least three measurements matching quality criteria.

Nanoparticle Calculations

Description of calculations made to obtain approximate IONP content (magnetite; Fe_3O_4) from Fe concentration measured by ICP-AES. In this study we used spherical IONPs with an average diameter of ca. 6.6 nm (Figure S2):

V (IONP) = $4/3\pi r^3 = 4/3\pi(3.2855 \times 10^{-7})^3 = 1.4856 \times 10^{-19}$ cm^3; ρ (magnetite) = 5.17 $g \cdot cm^{-3}$; m = ρ (magnetite) x V (IONP) = 7.6804×10^{-19} g

moles of Fe_3O_4= m / MW (Fe_3O_4) = $7.68 \times 10^{-19} / 231.533 = 3.3172 \times 10^{-21}$

moles of Fe = 3 x moles of Fe_3O_4 = 3 x $3.3172 \times 10^{-21} = 9.9516 \times 10^{-21}$

atoms of Fe per IONP = mole Fe in IONP • $N_A = 9.9516 \times 10^{-21} \bullet 6.022 \times 10^{23} = 5993$

Catalytic activity assay

The peroxidase-like activity of the mIONPs was studied by monitoring the oxidation of the peroxidase substrates TMB and OPD in the presence of H_2O_2, which yields a blue (λ = 652 nm) and yellow (λ = 450 nm) product respectively. The absorbance variation was monitored in the presence of the IONPs ([Fe] = 150 µM, for mIONPs; [Fe] = 550 µM for Ferumoxytol) or AuNPs ([Au] = 150 µM) nanocatalysts. The kinetic studies were performed in sodium acetate buffer (0.1 M, pH= 4.5, 5.5, 6.6) or PBS (0.01 M, pH = 7.4) in a total volume of 500 µL contained in quartz cuvettes (Hellma™; path length: 10 mm). The reactions were monitored spectrophotometrically at room temperature in time-scan mode. The Michaelis Menten kinetics assays were conducted with mIONP ([Fe] = 150 µM) in sodium acetate buffer (pH = 4.5) and in the presence of different concentrations of H_2O_2 (ranging from 0.060 to 30.3 mM) and TMB (ranging from 33.0 to 832 µM). The kinetic parameters were calculated fitting the absorbance data using Lineweaver–Burk plots of the Michaelis–Menten kinetics.

$$\frac{1}{v} = \frac{K_M}{V_{max}}\left(\frac{1}{[\mathrm{S}]} + \frac{1}{\mathrm{K}_M}\right)$$

Where v is the initial velocity, V_{max} is the maximal reaction velocity, [S] is the concentration of substrate and K_M is the Michaelis constant, and the turnover number (k_{cat}) was calculated from,

$$\mathrm{k_{cat}} = \frac{V_{max}}{[\mathrm{IONP}]}$$

Cell-to-cell contact co-culture

B16-F10(OVA) melanoma cells were seeded in 96-well plates at a density of 1.8×10^5 cells/cm^2 in a volume of 200 µL. After 24 h, B16-F10(OVA) formed a 100% confluent monolayer and 8.5 x 10^4 RAW264.7 macrophage cells were seeded on top (seeding density of 2.7×10^5 cells/cm^2) in a volume of 100 µL and allowed to adhere for 2 hours in complete medium (media mix ratio of RPMI-1640:DMEM = 7:1). Medium was removed, fresh RPMI-1640 medium was added and cells were allowed to settle for 30 minutes. Finally, medium was removed, treatment was added, and cells were incubated over 24 h. Due to the small number of cells employed, each condition was performed in triplicate and cells pooled for further analysis. Supernatants were collected and stored at -20˚C for further cytokine analysis. Cell viability assessment by flow cytometry was conducted by detaching RAW 264.7 and B16-F10(OVA) cells from the well with 100 µL of accutase® or trypsin, respectively. After 5 min at room temperature, the detachment solutions were neutralized with 100 µL of complete media. The resulting cell suspensions were washed with PBS and stained with 50 µL of Zombie Dye NIR diluted 1:100 in PBS over 45 min at 4° C in the dark. For differentiation between RAW 264.7 from B16-F10(OVA), cells were then washed with 0.1% BSA in PBS (and stained with Brilliant Violet-labeled anti-F4/80 antibody diluted 1:200 in the same buffer. Finally, the cell suspensions were washed with FACS buffer (1% FBS in PBS) by centrifugation (3 cycles, 800 g, 4 min) and suspended in 300 µL of the same buffer. Positive controls for necrotic cell death were heated to 80° C for 3 min prior to staining. Using a NovoCyte Flow Cytometer (ACEA Biosciences), cell populations were gated based on the forward and side scatter parameters and the not-single events leaved out based on forward area and height scatter parameters (FlowJo, LCC software). Differentiation between cells was based on F4/80-positive fluorescent staining found in RAW 264.7 cells. Necrotic cell populations were gated based on Zombie Dye NIR positive fluorescent staining. Results were normalized to the corresponding negative controls and expressed as mean ± SEM.

Transmembrane co-culture

RAW 264.7 macrophages were co-cultured with B16-F10(OVA) melanoma cells in transwell plates (24-well plate) separated by a 0.4 µm pore-size membrane. RAW264.7 cells were seeded on the apical chamber of the transwell plate at a density of 2.5×10^5 cells/cm^2 in a volume of 100 µL of complete DMEM medium and B16-F10(OVA) cells were seeded on the basolateral chamber of the well at a seeding density of 4.2×10^2 cells/cm^2 in a volume of 600 µL of complete RPMI 1640 medium. The cells were allowed to grow to 100% confluence for 48 h (final media mix ratio RPMI-1640:DMEM = 7:1). After removing the medium, cells were treated over 24 h with the different formulations. Transmembrane co-cultures were always accompanied by mono-culture controls exposed to the corresponding treatments used in the co-culture. For the mono-culture controls, 8×10^4 RAW 264.7 cells were seeded on the bottom of a 96-well plate (seeding density of 2.5×10^5 cells/cm^2) in a volume of 200 µL of media mix (RPMI-1640:DMEM = 7:1) and 8×10^4 B16-F10(OVA) cells were seeded on the bottom of a 24-well plate (seeding density of 4.2×10^2 cells/cm^2) in a volume of 700 µL of media mix (RPMI-1640:DMEM = 7:1). Cytokine and cell viability analysis was conducted as described before. In this case, no anti-F4/80 staining was needed as cells were physically separated by the well membrane.

Ferroptosis studies

B16-F10(OVA) or RAW 264.7 cells were seeded at 5×10^3 cells/well (seeding density of 1.6×10^4 cells/cm^2) in flat bottom 96-well plates and cultured for 24 h in 200 µL of complete medium. After removing the medium, cells were treated in quadruplicate with increasing concentrations of erastin (0, 0.63, 1.25, 2.5 µM) diluted in 100 µL of complete medium over

24 h. Then, and after removing erastin, cells were treated with mIONPs ([Fe] = 0.5 mM, 39 µg/mL of magnetite) in 100 µL of complete medium. Negative controls were treated with complete RPMI-1640 medium only. After a 24-hour exposure, medium was removed and 50 µL of MTT reagent in complete medium (0.5 mg/mL) was added to the cells and incubated for 2 h at 37° C. The supernatant was discarded and 100 µL of DMSO were added to solubilize the formazan crystals. Finally, the optical density of the samples was measured in a POLARstar Omega (BMG Labtech) microplate reader at 550 nm. Data was represented as the relative signal intensity to negative control, thus correlated to cell viability. Results are expressed as mean ± SEM.

Flow cytometric analysis of lipid hydroperoxides in live cells

B16-F10(OVA) cells were seeded at a seeding density of 4.5 x 10^4 cells/cm^2 in 24-well plate and incubated in complete RPMI 1640 media for 24 h at 37 ºC, 5% CO_2. Media was replaced with vehicle or erastin (1.25 mM; 0.63 mM; Cayman Chemical, Cambridge Bioscience, UK) in complete RPMI, and cells were incubated for 24 h at 37 ºC, 5% CO_2. Media was then replaced with vehicle control (7% H_2O nanopure water) or mIONPs ([Fe] = 1 mM, 77 µg/mL of magnetite) in complete RPMI and cells incubated for a further 24 h at 37 ºC, 5% CO_2. Cells were then treated with Liperfluo (10 µM; Dojindo Molecular Technologies Inc) or DMSO vehicle control (1%) for 30 min, at 37 ºC, 5% CO_2. As a positive control for lipid peroxides, cells were incubated with Cumene Hydroperoxide (100 µM; Sigma-Aldrich) in complete RPMI for 2 h at 37 ºC, 5% CO_2 prior to Liperfluo addition. Cells were detached using 100 µl accutase® and washed once with 5 ml FACS buffer**.** Using a NovoCyte Flow Cytometer (ACEA Biosciences), cell populations were gated based on the forward and side scatter parameters and the not-single events leaved out based on forward area and height scatter parameters (FlowJo, LCC software). Differentiation between cells was based on lipid peroxidation-positive fluorescent staining using Liperfluo® (530 nm laser).

Quantification of IL-6, IL-12, IL-10 and TNF-α cytokines by ELISA

Cytokines levels were measured in cell supernatants using sandwich ELISA following manufactures instructions. The optical density was measured in a POLARstar Omega (BMG Labtech) or in a TECAN Genios Pro 96/384 microplate reader at 450-550 nm. A 4-parameter sigmoidal (logistic) standard curve was used to quantify the cytokine present (GraphPad Prism software). Results are expressed as mean ± SEM in pg/mL or ng/mL, compared to untreated control wells.

Animals

Animals were cared for and handled in compliance with the Guidelines for Accommodation and Care of Animals (European Convention for the Protection of Vertebrate Animals Used for Experimental and Other Scientific Purposes) and internal guidelines, and all the experimental procedures were approved by the appropriate local authorities. All animals were housed in ventilated cages and fed on a standard diet *ad libitum*.

Radiolabelling of nanovaccines and SPECT/CT studies

IONVs were radiolabelled adopting synthesis-free method as previously described for related nanovaccines (Ščasnár and van Lier, 1993; Ruiz-de-Angulo *et al.*, 2016). In brief, after purification of purchased gallium-67 (Curium^{TM}, specific activity =1.4 TBq/µmol), 50 µL of IONPs (*ca.* 1 µM of magnetite) were mixed with 100 µL of $^{67}GaCl_3$ (*ca.* 37 MBq) and diluted up to 500 µL in acetate buffer (pH = 3.8 ± 0.1). Reaction was incubated over 30 min at 70° C and unbound gallium-67 was removed by two cycles of ultrafiltration (6708g for 10 min) through Amicon Ultracel (MWCO = 100 kDa) centrifugal devices, after what the retentate

was recovered in PBS (10 mM), ready to be injected. In order to assess the stability of the label, ^{67}Ga-IONP-TLRa/OVA micelles were incubated with a large excess of DOTA chelator as competitor for gallium atoms (10^6 moles of DOTA per mole of nanoparticle) at 37° C. At different time points, the samples were filtered again to separate radiolabelled micelles from DOTA-^{67}Ga complex. Depending on the activity, samples were measured using a CRC-25R dose calibrator (Capintec, USA) or a 2470 WIZARD^2 Automatic Gamma Counter (PerkinElmer). For *in vivo* imaging studies, tumour bearing C57BL/6 female mice (6-8 weeks old) were subcutaneously administered with 40 µL of ^{67}Ga-IONP-TLRa/OVA micelles (all injection ranged from 35 to 45 MBq). With the mouse under isoflurane anaesthesia (1.5−2% in oxygen), whole-body SPECT/CT scans were acquired at 3, 24 and 48 h after the injection using an eXplore speCZT CT scanner and an 8-slit collimator with a field of view of 32 and 78 mm in the transaxial and axial directions, respectively. With the full ring detector, 360° of data were acquired by rotating the collimator 45° (45 steps, 1°/step). Data were collected in an energy acquisition window from 125−150 keV to 84−102 keV and acquisition times from 60 min (80 s/step) to 45 min (60 s/step). The CT acquisition consisted of 220 views were acquired in 0.88° increments around the animal with 16 ms exposure per view. The X-ray tube settings were 70 kV and 32 mA. The SPECT images were reconstructed using the OSEM iterative algorithm (5 and 15 subsets, 3 and 5 iterations) into 128 × 128 × 32 array with a voxel size of 0.4 × 0.4 × 2.46 mm, and were not corrected for scatter and attenuation. The CT images were reconstructed using a cone beam filtered back-projection Feldkamp algorithm into 437 × 437 × 523 array with a voxel size of 0.2 × 0.2 × 0.2 mm. During image acquisition, mice were kept normothermic by the use of a heating blanket (Homeothermic Blanket Control Unit; Bruker BioSpin GmbH, Karlsruhe, Germany). After each SPECT scan, CT acquisitions were performed to provide anatomical information on each animal. For the quantification of SPECT images, PMOD image analysis software (PMOD Technologies Ltd, Zurich, Switzerland) was employed. Volumes of interest (VOIs) were drawn in major organs (namely, brain, lungs, heart, liver, kidneys, bladder and tumour) and those lymph nodes visible on the SPECT images, and the concentration of radioactivity was determined as counts per second per cubic centimetre (cps/cm^3). Values were normalised to the total amount of radioactivity present in the animal at t = 3 h. This value was determined by drawing a VOI on the whole animal. Values were finally expressed as percentage of injected dose (% ID) per cm^3. At the end of the scanning procedure, animals were sacrificed, and the organs of interest were removed for further *ex vivo* SPECT/CT imaging applying the same conditions of the *in vivo* images. Analysis of the injected dose percentage per gram of organ was performed by measuring their activity with the Gamma Counter.

Radiolabelling of immune checkpoint antibodies and immune-PET studies

For the detection of PD-L1 and OX40 expression *in vivo*, antibodies were radiolabeled with ^{89}Zr, which was produced in-house as [^{89}Zr]ZrC_2O_4 as previously reported (Zhang *et al.*, 2020). First, Abs were functionalised with the chelator. With that aim, the corresponding antibody was diluted with PBS to a final concentration of 2 mg/mL, the pH was adjusted to 8.7-9.0 with 0.1 M sodium carbonate and 5 equivalents of *p*-NCS-Bz-DFO (*p*-isothiocyanatobenzyl-desferrioxamine) were added. After 45 min incubation at 37 ºC the Abs were purified by spin filtration (12 000 rpm, 100 kDa, 6 min) and washed three times with PBS. The final protein concentration was determined by NanoDrop®. Radiolabelling of mAb-DFO with ^{89}Zr was performed by incubation with [^{89}Zr]ZrC_2O_4 in a 1 M oxalic acid solution. Therefore 50 or 500 µl of 1 M oxalic acid containing ^{89}Zr (ca. 37 MBq) were neutralized with 2 M sodium carbonate, 500 µg mAb was added and the volume adjusted to 0.5 or 1.0 mL with 0.5 M HEPES buffer. After 1 h incubation at room temperature the antibodies were purified by size exclusion chromatography (NAP5® or PD10®) and PBS.

The incubation and purification were monitored by iTLC. The radiochemical yield was 35-80%, depending on the batch of ^{89}Zr. PET imaging studies were conducted using PET in combination with computerized tomography (CT), using the β- and X-cube micro system of Molecubes. Static whole-body images (1 bed) were acquired in a 511 keV ± 30 % energetic window, with a total acquisition time of 10 min. PET images were analysed using PMOD image analysis software (PMOD Technologies Ltd, Zurich, Switzerland).

Tumour experiments

For the prophylactic approach, C57BL/6 female mice (6-8 weeks old) were immunized subcutaneously on day 0 and 14. One week after second immunization (day 21), 3×10^5 B16-F10(OVA) cells mixed with Matrigel® Matrix (volume ratio of 2:1) were implanted in the right back of mice. On the other hand, in the therapeutic strategy mice were subcutaneously injected with the melanoma cancer cells and then treated on days 7, 10 and 13 after tumor challenge. In order to compare IONP-filled micelles with Ferumoxytol, B16-F10(OVA) cancer cells were co-administered together with the treatment. Finally, when immune checkpoint inhibitors were used, therapy regime was slightly changed: nanovaccines were subcutaneously injected on days 4, 11 and 18 after tumor implantation and, 1 and 4 days after each treatment, monoclonal antibodies blocking PD-L1 (100 μg, intraperitoneal) and/or activating OX40 (10 μg, intratumoral) were administered. In all cases, animals were monitored for tumor growth every two days using an electronic caliper 779A series (starrett). Criteria for humane endpoint included tumors greater than 1.5 cm diameter or ulceration.

Tissue processing protocols

Bone marrow derived dendritic cell (BMDC) primary culture. C57BL/6 female mice (6−12 weeks old) were sacrificed by cervical dislocation and intact femurs and tibiae of hind limbs were removed. Bones were washed in cold PBS (10 mM) and bone marrow was flushed with the same buffer using a syringe as described previously (Lutz *et al.*, 1999). After the erythrocytes were lysed, the cells were washed and resuspended in RPMI-1640 supplemented with penicillin (100 μg/mL), Streptomycin (100 μg/ mL), L-glutamine (2 mM) and heat inactivated FBS (10%). On day zero cells were plated at a concentration of 2×10^6 cells per 100 mm bacteriological Petri dish (Falcon) in 10 mL of media supplemented with 20 ng/mL of murine GM-CSF (Peprotech) and maintained in a humidified incubator with 37° C and 5% CO_2. On day 3, 10 mL of complete RPMI media containing GM-CSF (20 ng/mL) was added to each Petri dish. On day 6, half of the supernatant was collected, centrifuged and cell pellet resuspended in 10 mL of fresh complete RPMI with GM-CSF (10 ng/mL) and added again to each Petri dish. Finally, on day 8 cells were harvested for further analysis.

Purification of Peripheral Blood Cells. To analyse the circulating T cells immune response, blood was taken (100 μL) via the facial vein and diluted up to 4 mL in cold PBS (10 mM). After centrifugation (1028g, 5 min at 4° C), the pellet was resuspended in 5 mL of RBC lysis buffer and incubated at room temperature for 5 min while vortexing vigorously. The lysis was quenched by addition of 8 mL of 5% FBS in PBS (10 mM) and mixture was washed twice, ready for further analysis.

Splenocytes, lymphocytes and tumour-infiltrating immune primary cultures. Spleens, TDLN and tumour tissue were perfused with tissue dissociating mix (3, 2.5 and 5 mL of collagenase/DNase I in RPMI-1640, respectively), cut into small pieces and incubated for 30 min at RT. After stopping the reaction with 500 mM EDTA, organs were smashed with the plunger of a syringe and resulted cell suspension collected into falcons after removing big tissue clamps. Red blood cell lysis was performed by adding RBC lysis buffer to cell pellets and incubating at RT (2 mL over 5 min for spleens and 1 mL over 1 min for tumours). Cells

were washed twice with 8 mL of 5% FBS in PBS (10 mM) and resuspended in 2 mL of complete RPMI-1640 ready to use.

***In vitro* experiments with dendritic cells**

The study of DCs activation when incubated with IONP-filled micelles or TLRas was conducted using primary culture of bone marrow derived dendritic cells (BMDCs). Differentiated BMDCs were resuspended in complete RPMI-1640 and plated at a final concentration of 2×10^5 cells/well (0.1mL/well) in round-bottom (activation markers) or flat-bottom (cytokines) 96-well plates. Each formulation was diluted accordingly in media and added to cells (0.1 mL), in triplicate. 24 h after, supernatants were harvested for further cytokine analysis. Cell viability of BMDCs was measured using the MTT assay as previously described. To analyze the activation markers on DC surface, cells were washed twice with PBS buffer and stained with Alexa Fluor 488-labeled anti-CD11c, PerCP-Cy5.5-labeled anti-IA/IE, Brilliant Violet 421-labeled anti-CD80, PE-labeled anti-CD86, and APC-labeled anti-PD-L1 antibodies. Using a FACS Canto II flow cytometer (BD Bioscience), cells were electronically gated based on the forward and side scatter parameter and the not-single events leaved out based on forward area and height scatter parameters (FlowJo, LCC software). DCs were gated based on positive staining for CD11 population marker, where the relative mean fluorescence intensity (MFI) of each marker was analyzed. Isotype controls were included in each assay and are not showed in the figures for clarity purposes. Experiment was conducted three times.

Assessing immune responses *in vivo*

In order to study the immune response after immunization and tumor challenge, C57BL/6 female mice were administered subcutaneously with 5 µg of OVA, 12 µg of polyIC and 4 µg of R837 alone or in combination with IONP micelles (78 µg of magnetite) on day 0 and 14. 21 days after first immunization, mice were challenged with 3×10^5 B16-F10(OVA) melanoma cells and, after 63 days (84 days after the beginning of the experiment) re-challenged with another 3×10^5 B16-F10(OVA) tumor cells. Mice were culled by cervical dislocation 128 days after first administration and blood samples and spleens harvested for the analysis of the generated immune response. Both splenocytes and blood cells were analyzed for SIINFEKL-specific $CD8^+$ T cells and effector memory $CD8^+$ T cells. 1×10^6 cells were plated in round-bottom 96-well plates and washed with 5% FBS in PBS (10 mM). Cells were stained with Brilliant Violet 421-labeled anti-CD3, PE.Cy7-labeled anti-CD8, APC-labeled anti-CD44, FITC-labeled anti-CD62L and PE-labeled H-$2k^b$-$OVA_{257-264}$ dextramer (Immudex). SIINFEKL specific cell percentage was analyzed in the $CD8^+$ T cell population ($CD3^+$ and $CD8^+$ double positive) or in the effector memory $CD8^+$ T cell population (inside $CD3^+$ and $CD8^+$ double positive population, cells showing a phenotype of $CD44^{high}$ and $CD62L^{low}$). In order to analyze the intracellular cytokine production by flow cytometry, 1 x 10^6 splenocytes were seeded also in round-bottom 96-well plates but diluted in complete RPMI media (0.1 mL/well). Another 0.1 mL were added per well containing the BD GolgiStop™ Protein Transport Inhibitor (1.4 µg/mL of Monensin), the PE-labelled anti-CD107a antibody (LAMP-1 protein) and 10 µg/mL of SIINFEKL diluted in media. After 5 h incubation at 37° C, cells were washed and stained with Brilliant Violet 421-labeled anti-CD3, FITC-labeled anti-CD8 and Brilliant Violet 510-labeled anti-CD4. Then cells were fixed and permeabilized using the commercially available BD Cytofix/Cytoperm fixation and permeabilisation kit and intracellularly stained with APC-labeled anti-IFN-y and PE.Cy7-labeled anti-TNF-α. Cells were gated based on double positive for CD3 and CD8 markers, excluding $CD4^+$ cells and vice versa. Intracellular cytokines and degranulation marker were analyzed in $CD3^+CD4^+$ or $CD3^+CD8^+$ double positive cell populations. Isotype controls were

included and were not showed in the figures for clarity purposes. Results were expressed as mean ± SEM of at least 3 mice per group of immunization and compared to unstimulated wells.

Analysis of immune cells phenotype *in vivo*

For the study of OX40 positive immune cells *in vivo* C57BL/6 female mice were injected with 3×10^5 melanoma cells in the back and, 8 days later, animals were sacrificed and organs of interest harvested (see Supplemental Information for tissue processing description). 1×10^6 cells were plated in round-bottom 96-well plates and washed with FACS buffer. Cells were stained with Brilliant Violet 421-labeled anti-CD3, Brilliant Violet 510-labeled anti-CD4, PE.Cy7-labeled anti-CD8, APC-labeled anti-CD44, FITC-labeled anti-CD25 and PerCP-Cy5.5-labeled anti-OX40. Expression of OX40 marker was analyzed in $CD3^+$ and $CD4^+$ T cells. CD44 and CD25 activation markers were used to analyze the phenotypic differences between OX40 positive and negatives T cells. The analysis of PD-L1 expression in B16-F10(OVA) melanoma cells was analysed by staining the cells with APC-labeled anti-PD-L1.

Statistical analysis

Data presented as mean ± SEM. The differences between the control and the experimental groups were assessed using two-tailed unpaired Student's t tests and the differences among groups > 2 by one-way ANOVA (GraphPad Prism, GraphPad Software, La Jolla, CA). Statistical significance was set at $*p < 0.05$; $**p < 0.01$; $^{\#}p < 0.001$, as indicated in the figure legends. All *in vivo* experiments were repeated at least twice with a minimum of five mice per group and the *in vitro* studies a minimum of three times.

References

Bocanegra Gondan, A. I. *et al.* (2018) 'Effective cancer immunotherapy in mice by polyIC-imiquimod complexes and engineered magnetic nanoparticles', *Biomaterials*, 170, pp. 95–115.

Carion, O. *et al.* (2007) 'Synthesis, encapsulation, purification and coupling of single quantum dots in phospholipid micelles for their use in cellular and in vivo imaging.', *Nature Protocols*, 2(10), pp. 2383–2390.

Garaikoetxea Arguinzoniz, A. *et al.* (2015) 'Enhanced cancer cell killing of a Pt(iv) prodrug promoted by outer-sphere coordination with polyethyleneimines', *Dalton Transactions*, 44(16), pp. 7135-38.

Gomez Blanco, N. *et al.* (2012) 'Iron oxide-filled micelles as ligands for fac-[M(CO)3]+ (M = (99m)Tc, Re).', *Chemical communications (Cambridge, England)*. The Royal Society of Chemistry, 48(35), pp. 4211–3.

Lutz, M. B. *et al.* (1999) 'An advanced culture method for generating large quantities of highly pure dendritic cells from mouse bone marrow', *Journal of Immunological Methods*, 223(1), pp. 77–92.

Moros, M. *et al.* (2010) 'Engineering biofunctional magnetic nanoparticles for biotechnological applications', *Nanoscale*. The Royal Society of Chemistry, 2(9), p. 1746.

Ruiz-de-Angulo, A. *et al.* (2016) 'Microdosed Lipid-Coated 67 Ga-Magnetite Enhances Antigen-Specific Immunity by Image Tracked Delivery of Antigen and CpG to Lymph Nodes', *ACS Nano*. American Chemical Society, 10(1), pp. 1602–1618.

Ščasnár, V. and van Lier, J. E. (1993) 'The use of SEP-PAK Sl cartridges for the preparation of gallium chloride from the citrate solution', *European Journal of Nuclear Medicine*, 20(3), pp. 273–273.

Song, W.-J. *et al.* (2010) 'Gold nanoparticles capped with polyethyleneimine for enhanced siRNA delivery.', *Small (Weinheim an der Bergstrasse, Germany)*, 6(2), pp. 239–246.

Sun, S. *et al.* (2004) 'Monodisperse MFe2O4 (M = Fe, Co, Mn) nanoparticles.', *Journal of the American Chemical Society*, 126(1), pp. 273–279.

Thomas, M. and Klibanov, A. M. (2003) 'Conjugation to gold nanoparticles enhances polyethylenimine's transfer of plasmid dna into mammalian cells', *Proceedings of the National Academy of Sciences of the United States of America*. National Academy of Sciences, 100(16), pp. 9138–9143.

Traini, G. *et al.* (2019) 'Cancer Immunotherapy of TLR4 Agonist-Antigen Constructs Enhanced with Pathogen-Mimicking Magnetite Nanoparticles and Checkpoint Blockade of PD-L1', *Small*. John Wiley & Sons, Ltd, 15(4), p. 1803993.

Zhang, Y. *et al.* (2020) 'PLGA protein nanocarriers with tailor-made fluorescence/MRI/PET imaging modalities', *Nanoscale*. Royal Society of Chemistry (RSC), 12, pp. 4988–5002.

Supplemental data items

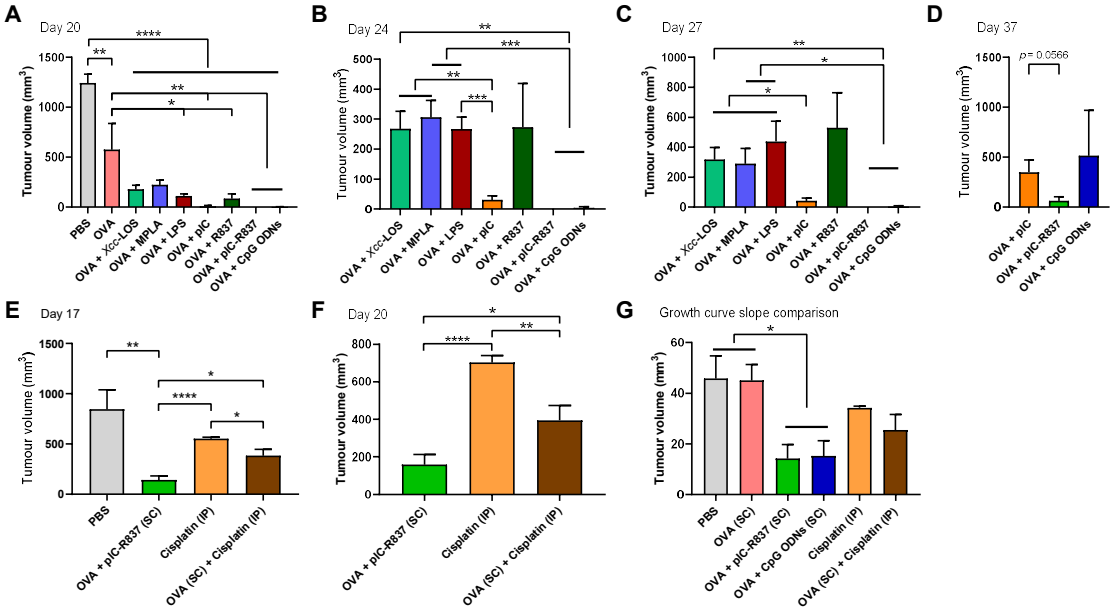

Figure S1. Statistical analysis of tumour growth curves. * $P < 0.05$, ** $P < 0.01$, *** $P < 0.001$, **** $P < 0.0001$ by one-way ANOVA followed by Tukey's test for days where all animals were still alive (A) and by two-tailed unpaired Student's t-test for days where any group was already missing (B-F). G) Linear regression of each tumour growth curve showed in Figure 1D was performed and the mean value of the slopes of each experimental group compared by one-way ANOVA followed by Tukey's test. Related to Figure 1.

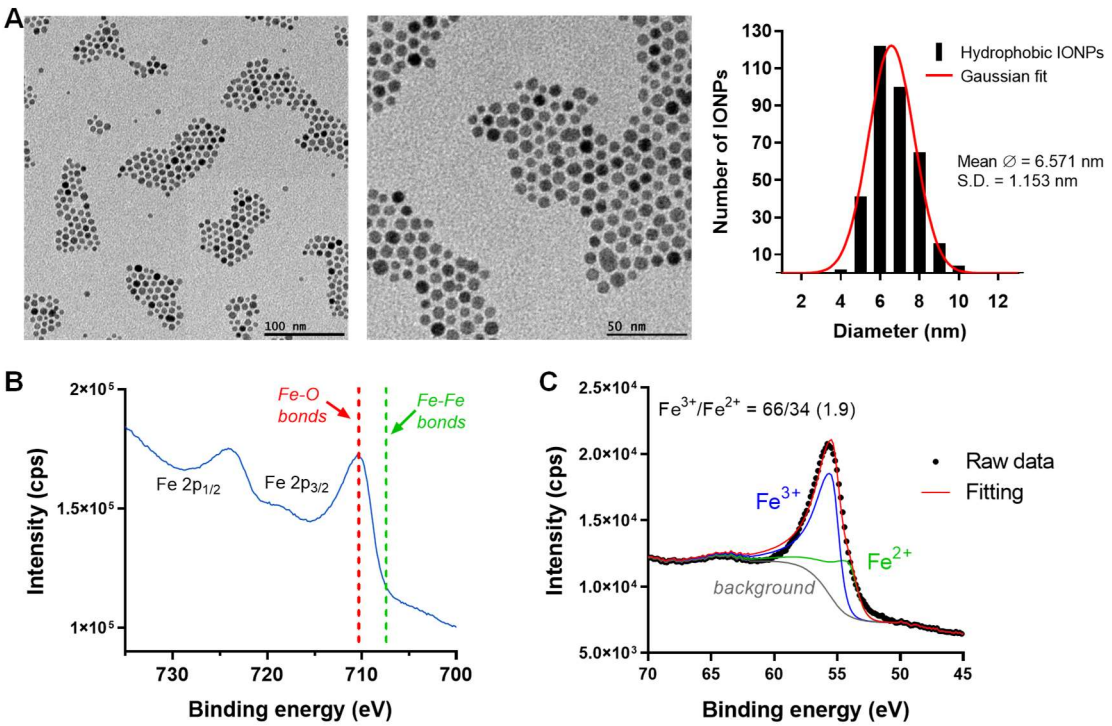

Figure S2. Characterization of hydrophobic IONPs employed in this work. A) Representative TEM images and size distribution of more than 300 IONPs. XPS spectra of B) Fe 2p and C) Fe 3p. Related to Figures 2-8 and Figure 10.

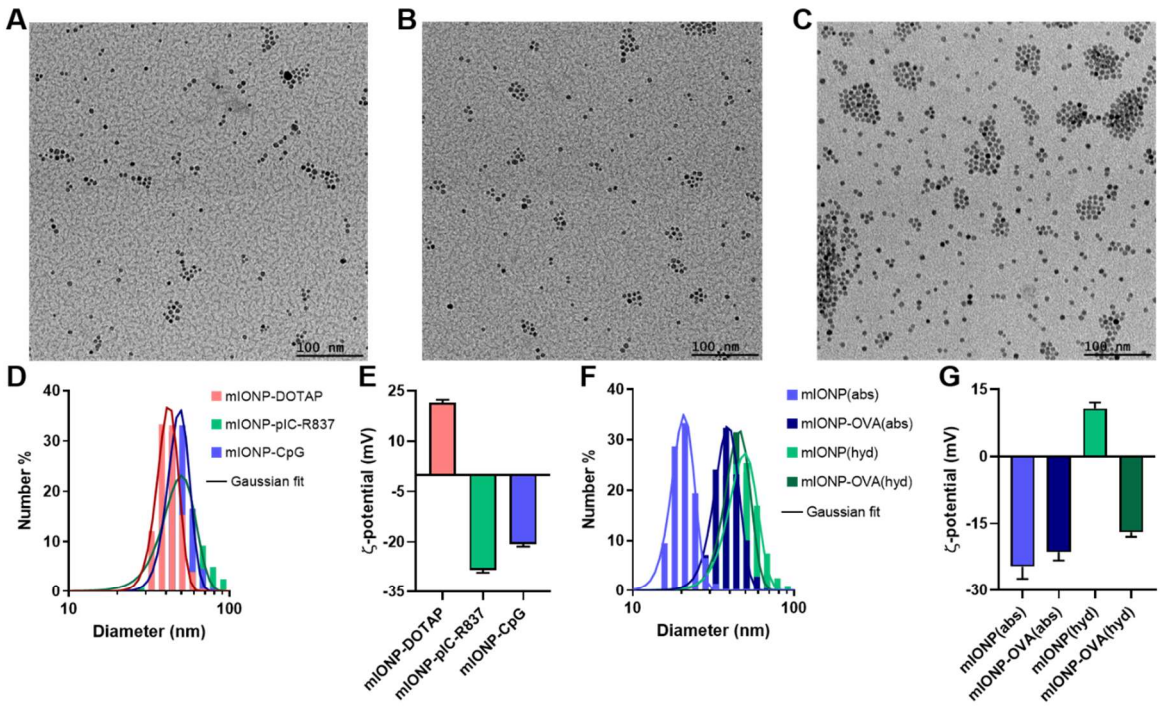

H

	mIONP-DOTAP micelles	mIONP-pIC-R837	mIONP-CpG
Mean ø (nm)	41.86	50.15	48.95
SD (nm)	6.319	11.46	7.578
PDI	0.471 ± 0.01	0.381 ± 0.01	0.422 ± 0.01
Z-potential (mV)	21.5	-28.4	-20.6

I

	mIONP(abs) micelles	mIONP-OVA(abs)	mIONP(hyd) micelles	mIONP-OVA(hyd)
Mean ø (nm)	20.19	38.93	49.43	45.58
SD (nm)	3.337	6.699	9.947	8.071
PDI	0.313 ± 0.01	0.266 ± 0.02	0.230 ± 0.02	0.478 ± 0.10
Z-potential (mV)	-24.6	-27-4	10.8	-16.9

Figure S3. Characterization and biofunctionalization of magnetite-filled micelles. A-C) Representative TEM images of iron oxide-based micelles: A) DPPE-mPEG(2000):DOTAP stabilized mIONPs and PEG-PL-coated for OVA B) absorption (DSPE-cPEG(2000) with COOH end groups) and C) covalent anchoring by hydrazone linkages (DSPE-aPEG(2000) with NH_2 end groups). D-I) Hydrodynamic size distribution and zeta potential of functionalized micelles measured by DLS. Related to Figures 2-8 and Figure 10.

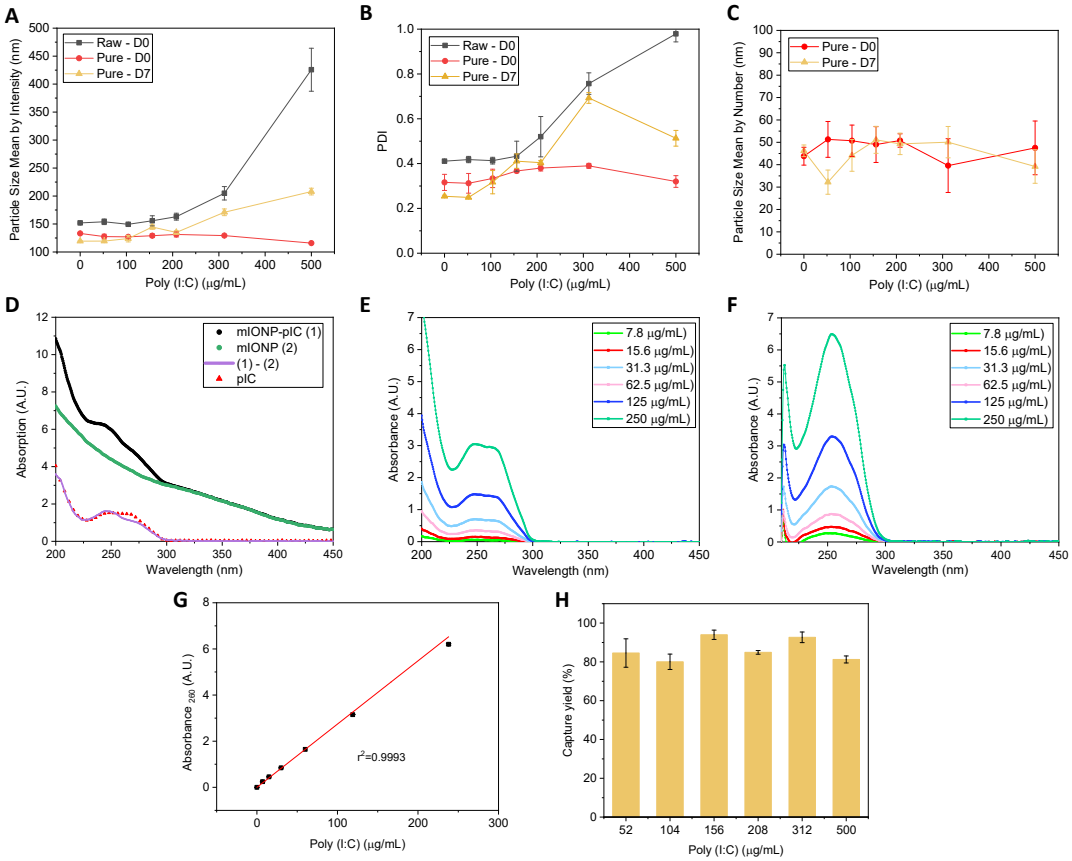

Figure S4. Hydrodynamic size characterization by DLS of DPPE-mPEG(2000):DOTAP stabilized IONP functionalized with increasing amounts of pIC (mIONP-pIC), just after synthesis and after purification at days 0 and 7 stored at 4° C: A) particle size mean by intensity and B) polydispersity index (PDI); C) particle size mean by number after purification. Data are presented as an average of three readouts. D) Absorbance spectra comparison between mIONP-DOTAP and mIONP-pIC after purification, indicating the effective capture of pIC. E) Typical pIC absorption spectra. F) pIC absorption peaks after digestion in basic environment (λ = 260 nm) and G) linear regression made to determine the H) pIC capture yield in the mIONPs surface (%). Related to Figures 2-8 and Figure 10.

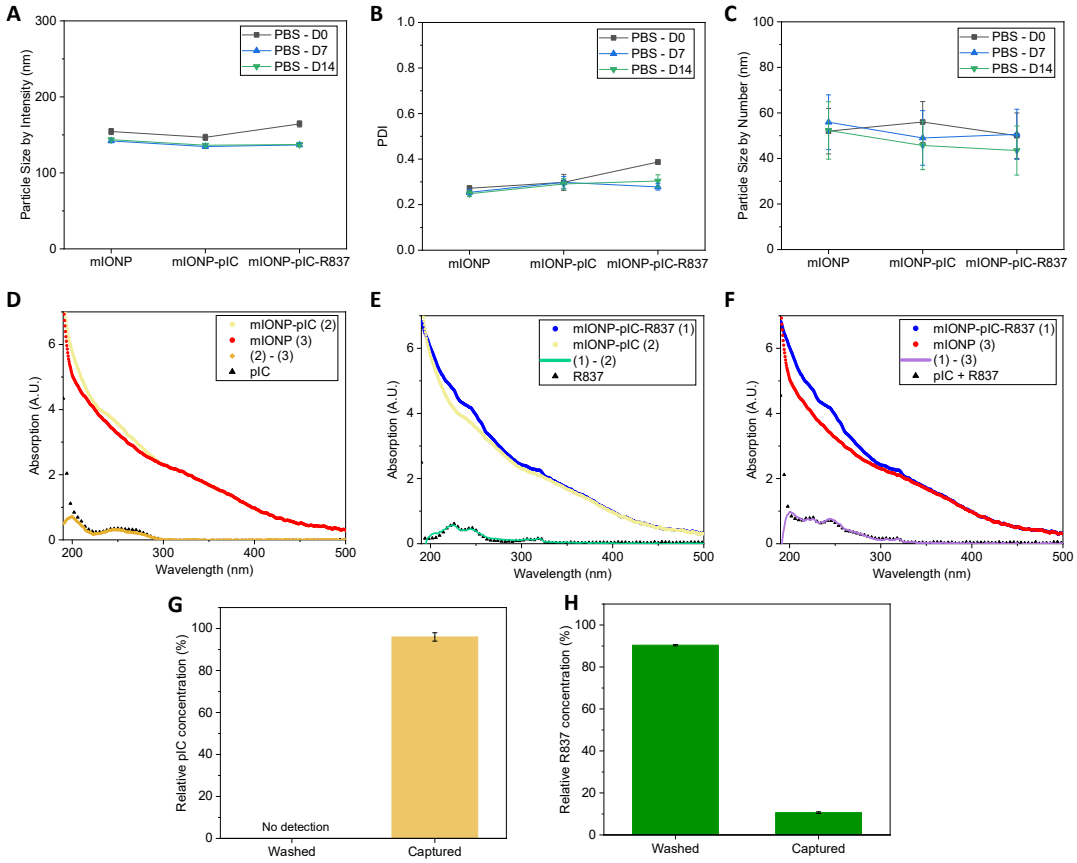

Figure S5. Characterization of DPPE-mPEG(2000):DOTAP-coated IONP micelles functionalized with pIC and R837 (mIONP-pIC-R837). A-C) Hydrodynamic size characterization by DLS of mIONP-pIC-R837 micelles, after synthesis and purification at days 0, 7 and 14 in PBS at 4° C: A) particle size mean by intensity, B) polydispersity index (PDI), and C) particle size mean by number. Data are presented as an average of three readouts. Absorbance spectra comparison between D) mIONP-DOTAP and mIONP-pIC, E) mIONP-pIC-R837 and mIONP-pIC, and F) and mIONP-pIC-R837 and mIONP after purification, indicating the effective capture of both pIC (31 µg/mL) and R837 (5 µg/mL). Final capture yield (%) of G) pIC (measured upon basic digestion) and H) R837 (measured at $\lambda = 320$ nm prior to digestion). Related to Figures 2-6, Figure 8 and Figure 10.

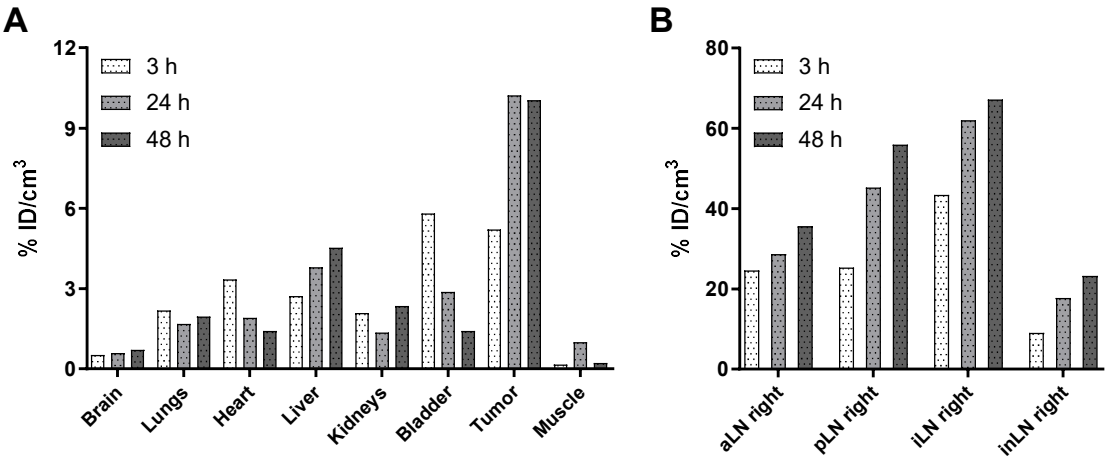

Figure S6. Dynamics of ^{67}Ga-labeled mIONP-CpG ODN nanovaccine over the different experimental time points. Radiolabeled mIONP-CpG ODNs (23.6 µg of magnetite, 43.4 MBq) were injected into the hock of tumour bearing mice and *in vivo* acquired images were analysed using PMOD software, at 3, 24 and 48 h after administration. Related to Figure 2.

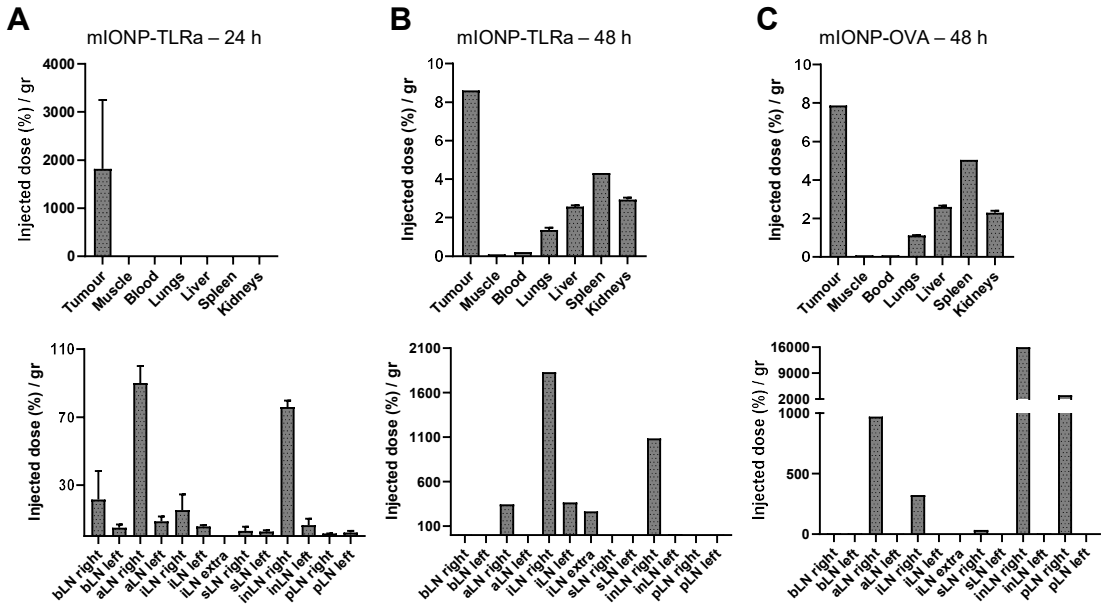

Figure S7. Biodistribution analysis of differently functionalized nanovaccines administered subcutaneously in tumour bearing mice. A) mIONP-pIC-R837 micelles administered peritumorally (4.68 µg of magnetite, 34.8 MBq) and analyzed after 24 h; B) mIONP-CpG micelles injected in the right flank (23.6 µg of magnetite, 42.2 MBq, 48 h); and C) mIONP-OVA micelles injected in the right hind limb (hock, 15.6 µg of magnetite, 40.7 MBq, 48h). bLN, brachial LN; aLN, axillary LN; iLN, iliac LN; sLN, sciatic LN; inLN, inguinal LN; pLN, popliteal LN. Related to Figure 2.

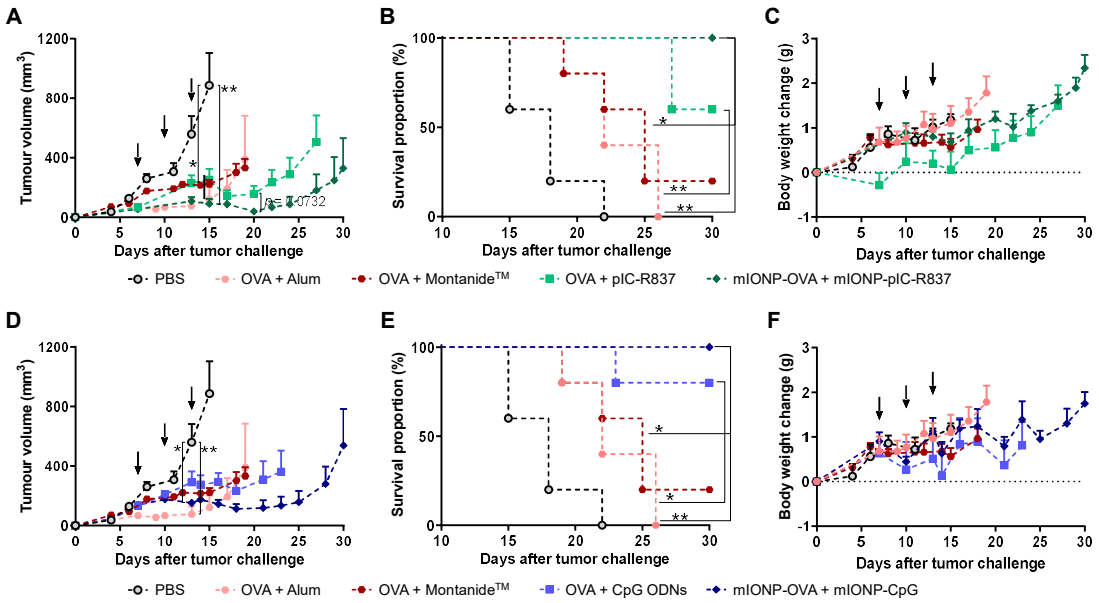

Figure S8. Incorporation of TLRa/OVA into IONP-filled micelles enhances the therapeutic outcome of antigen/adjuvant immunotherapy. C57BL/6 mice (n = 5) were treated on day 7, 10 and 13 after B16-F10(OVA) cells injection in the right back. Animals were subcutaneously administered (hock) with 10 µg of OVA in combination with adjuvants suitable for human vaccines (Alum, Montanide™ (1:1 volume ratio with antigen solution)) and either with A-C) pIC-R837 (4 and 2 µg, respectively) or D-F) CpG ODNs (10 µg) loaded into IONP-filled micelles (119 µg magnetite). A, D) Average tumour growth curves; B, E) Kaplan-Meier survival curves; and C, F) animal body weight change over the experiment. Arrows indicate the days of therapy administration. Data are showed as mean ± SEM. * $P < 0.05$, ** $P < 0.01$ by two-tailed unpaired Student's t-test (A, D) and by Log-rank (Mantel-Cox) test (B, E) between the indicated groups. Related to Figure 3.

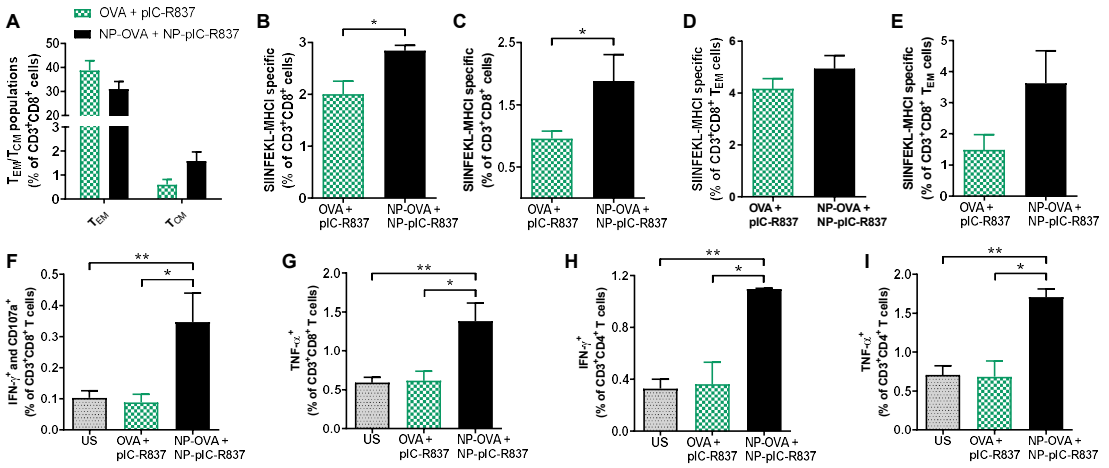

Figure S9. Long-term adaptive immune response elicited by nanovaccines. C57BL/6 female mice (n = 5) were subcutaneously immunized with 5 µg of OVA, 12 µg of polyIC, 4 µg of R837 alone or adsorbed to mIONPs on day 0 and 14 and, on day 21 were challenged with 3 x 10^5 B16-F10(OVA) cells. On day 84 after first immunization, animals were rechallenged with melanoma cells in the contralateral side. Six weeks later, mice were sacrificed, and blood and spleens were collected for further immune analysis. A) Effector (T_{EM}) and central memory (T_{CM}) $CD8^+$ T cell percentages in spleen. SIINFEKL-specific (B, C) $CD8^+$ and (D, E) T_{EM} cells in (B, D) spleen and (C, E) blood. (F-I) Intracellular IFN-γ and TNF-α production and CD107a expression in (F, G) $CD8^+$ and (H, I) $CD4^+$ T cells after 5 h of incubation with 10 µg/mL of SIINFEKL peptide. * $P<0.05$, **$P<0.01$, by one-way ANOVA followed by Tukey's test. Related Figure 3.

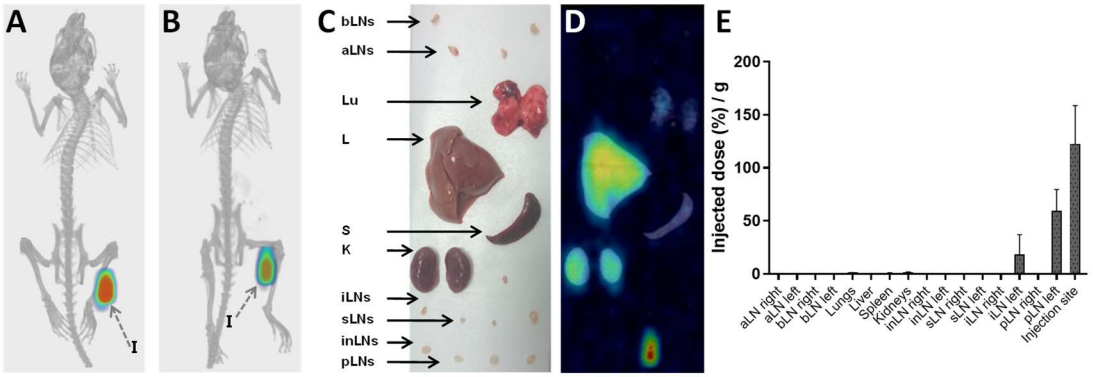

Figure S10. Changes in size of the micelles modified drastically the biodistribution of the vaccine. C57BL/6 mice (n = 2) were administered with mIONP-big micelles (9.2 µg of magnetite, 2.65 MBq) subcutaneously in the left hock. SPECT/CT images of representative mouse A) 3 h and B) 24 h after injection. C) Photograph of selected harvested organs, D) SPECT/CT images of the extracted organs and E) biodistribution expressed as injected dose percentage per gram of tissue. bLN, brachial LN; aLN, axillary LN; Lu, lungs; L, liver; S, spleen; K, kidneys; iliac LN; sLN, sciatic LN; inLN, inguinal LN; pLN, popliteal LN; injection site (I). Related Figure 3.

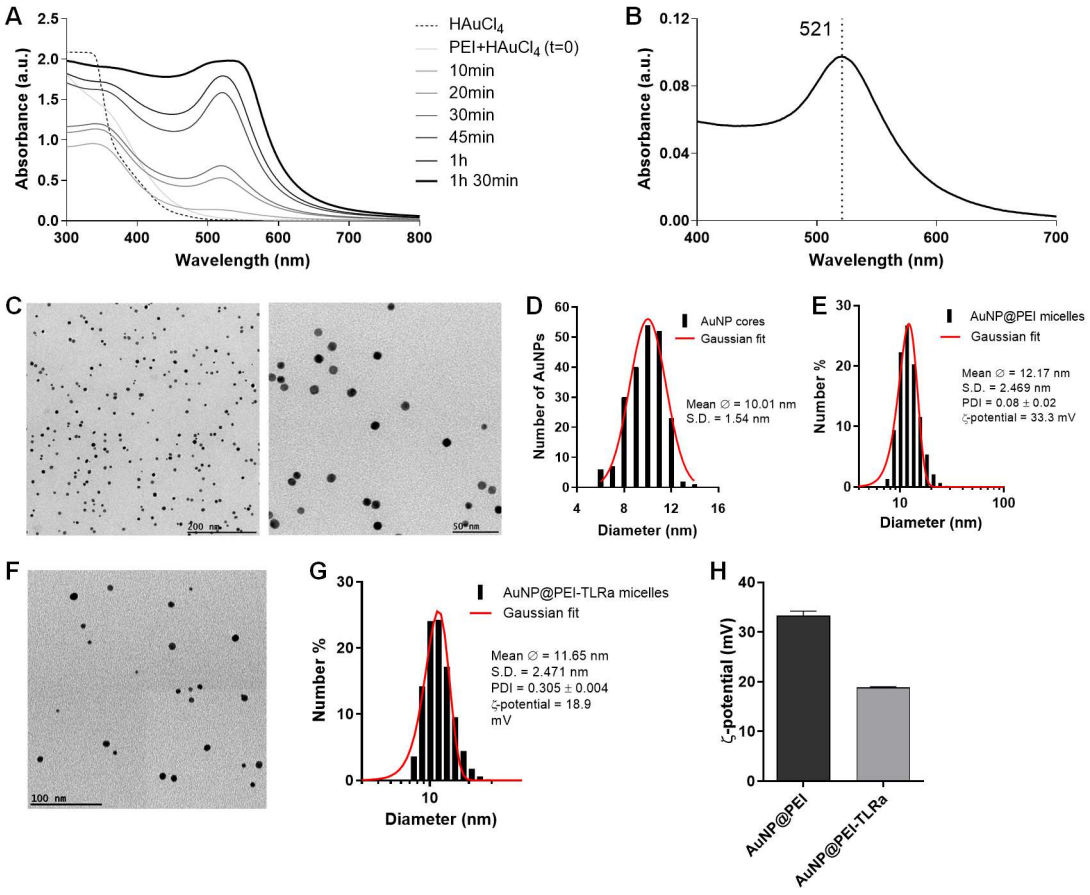

Figure S11. Characterization of PEI-capped AuNP micelles. A) UV-vis spectra of the solutions of HAuCl4 and 1.8 kDa PEI at different stages of the synthesis in water and B) the spectrum showing the surface plasmon resonance band at 521 nm. C) Representative TEM images, D) size distribution of more than 300 NPs, and E) hydrodynamic diameter analyzed by DLS. F-H) AuNP@PEI-TLRa system characterization showing F) a representative TEM image, G) hydrodynamic diameter measured by DLS and H) zeta potential values before and after functionalization with TLRas. Related to Figure 6.

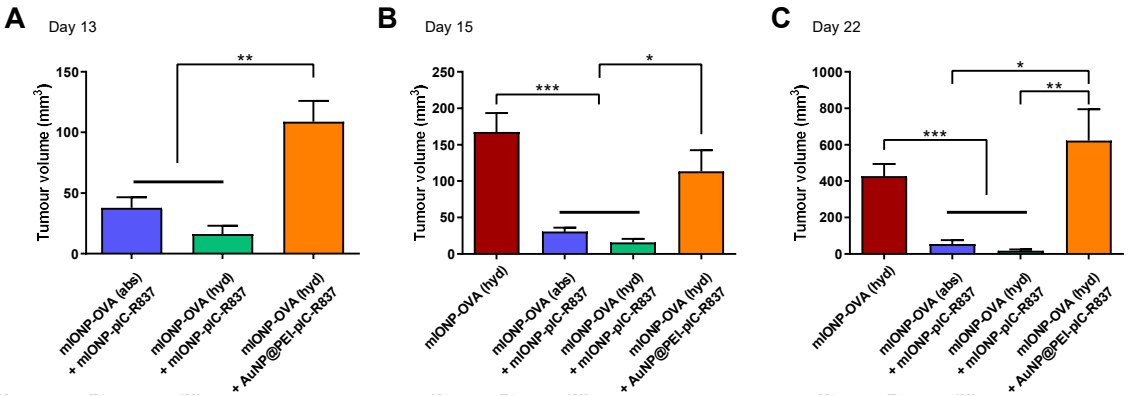

Figure S12. Statistical analysis of tumour growth curves. * $P < 0.05$, ** $P < 0.01$, *** $P < 0.001$ by two-tailed unpaired Student's t-test at days A) 13, B) 15, and C) 22 after tumour inoculation. Related to Figure 6.

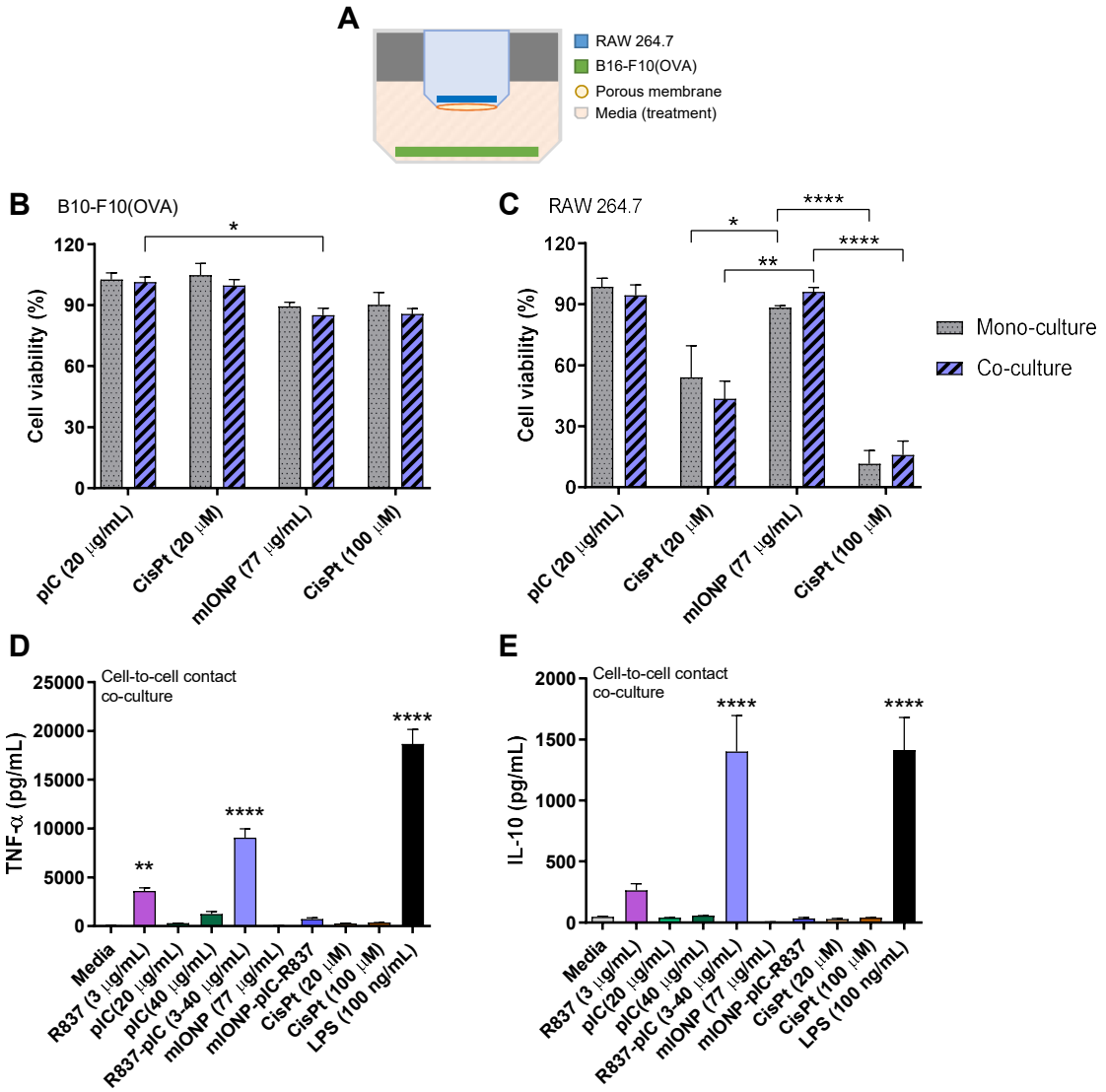

Figure S13. Melanoma B16-F10(OVA) and RAW 264.7 macrophage cells co-culture (transmembrane and cell-to-cell contact) experiments. A) Schematic representation of B16-F10(OVA) and RAW 264.7 transmembrane co-culture set-up. Comparison of B) B16-F10(OVA) and C) RAW 264.7 cell viability in mono-culture (M, solid bars) or transmembrane co-culture (C, striped bars), represented as subtraction from normalized necrotic cell death triggered upon treatment. Cytokine levels elicited upon treatment under cell-to-cell contact co-culture approaches for D) TNF-α and E) IL-10**.** 77 μg/mL magnetite = 1 mM of Fe. Data are shown as mean ± SEM (n =3). * $P < 0.05$, ** $P < 0.01$, **** $P < 0.0001$ by B, C) two-way ANOVA followed by Tukey's test and D, E) one-way ANOVA followed by Dunnett's test. Related to Figure 8.

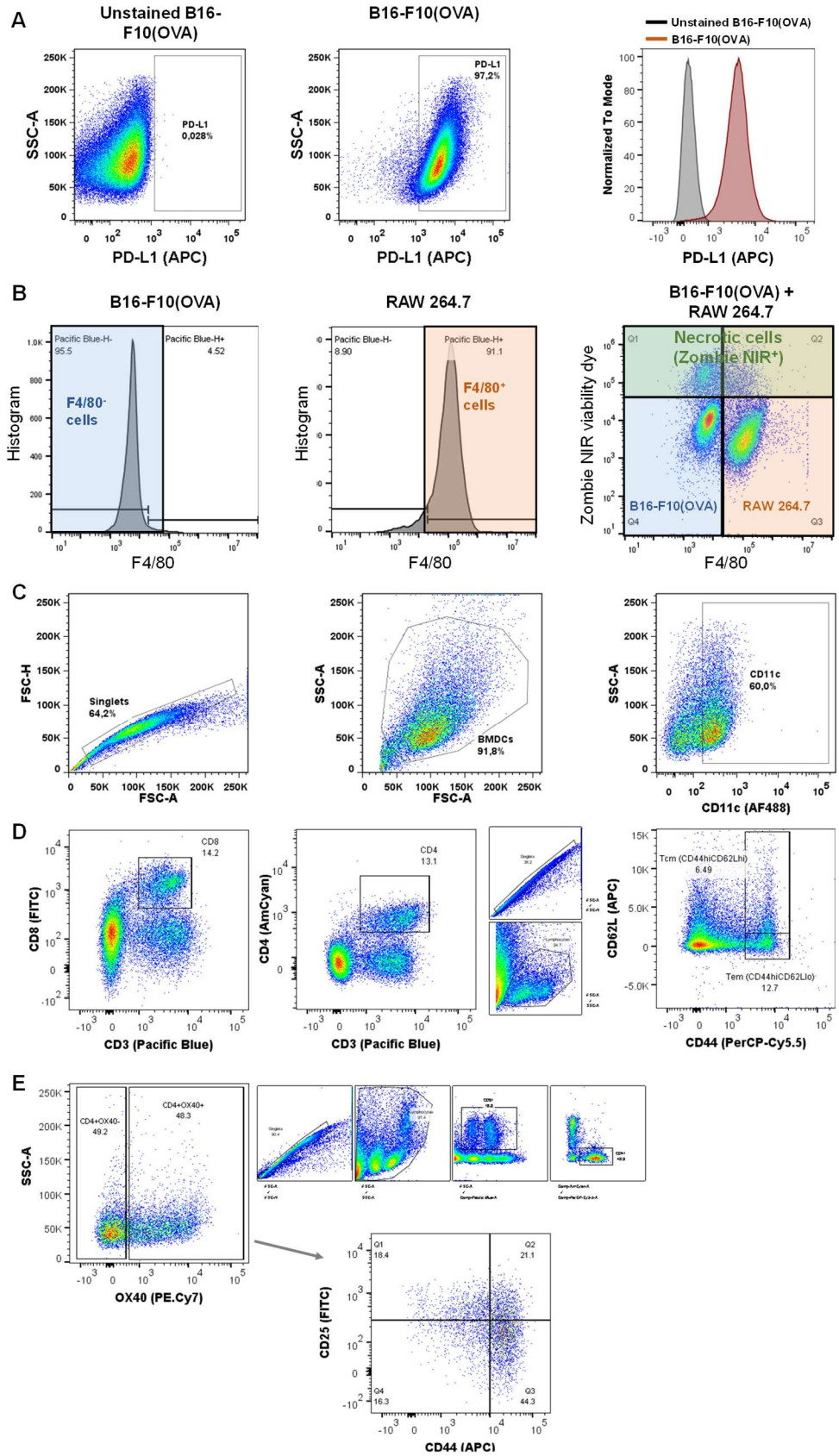

Figure S14. Cell gating strategy employed over this work. A) PD-L1 expression in B16-F10(OVA) mouse melanoma cells analyzed by flow cytometry. B) Cell viability as necrotic development in cell-to-cell co-cultures of B16-F10(OVA) melanoma and RAW 264.7 cells;

C) DCs population defined as $CD11c^+$ cells; T cells gating for D) immune response analysis and E) tumour-infiltrating immune cells analysis. Related to Figures 1, 3, 6, 8, 9 and 10.